

# Multichrome encoding-based multiplexed, spatially resolved imaging reveals single-cell RNA epigenetic modifications heterogeneity

Received: 29 January 2024

Accepted: 14 January 2025

Published online: 22 January 2025



Dongsheng Mao<sup>1,4</sup>, Xiaochen Tang<sup>2,4</sup>, Runchi Zhang<sup>1</sup>, Song Hu<sup>3</sup>, Hongquan Gou<sup>1</sup>, Penghui Zhang<sup>3</sup>, Wenxing Li<sup>1</sup>✉, Qiuhui Pan<sup>2</sup>✉, Bing Shen<sup>1</sup>✉ & Xiaoli Zhu<sup>1</sup>✉

Understanding the heterogeneity of epigenetic modifications within single cells is pivotal for unraveling the nature of the complexity of gene expression and cellular function. In this study, we have developed a strategy based on multichrome encoding and “AND” Boolean logic recognition for multiplexed, spatially resolved imaging of single-cell RNA epigenetic modifications, termed as PROximity Exchange-assisted Encoding of Multichrome (PREEM). Through the implementation of this strategy, we can now map the expression and nuclear distribution of multiple site-specific RNA N<sup>6</sup>-methyladenosine (m<sup>6</sup>A) modifications at the single-molecule resolution level in single-cells, and reveal the previously unknown heterogeneity. Notably, we demonstrate how these patterns change after treatment with various drugs. Moreover, cyclic imaging with tailed DNA self-assembly further suggest the scalability and adaptability of PREEM’s design. As an innovative epigenetic modification imaging tool, PREEM not only broadens the horizons of single-cell epigenetics research, enabling joint analysis of multiple targets beyond the limitations of imaging channels, but also reveals cell-to-cell variability, thereby enhancing our capacity to explore cellular functions.

To date, more than 100 different kinds of RNA modifications have been characterized, which play an important role in shaping an epitranscriptomic landscape of gene expression<sup>1,2</sup>. Among them, N<sup>6</sup>-methyladenosine (m<sup>6</sup>A) stands out as the most abundant internal RNA modification<sup>3</sup>, with its dynamic and reversible regulation playing a pivotal role in developmental regulation and disease development (e.g., cancers, neurodegenerative diseases, and metabolic disorders)<sup>4,5</sup>. Methylation of individual RNA molecules at the single-cell level is crucial for gaining detailed insights into molecular mechanisms, facilitating our understanding of single-cell heterogeneity. However, a significant challenge in such studies lies in the scarcity of techniques capable of providing precise, in-situ location information concerning

m<sup>6</sup>A modification<sup>6</sup>. Furthermore, the coexistence of multiple m<sup>6</sup>A RNAs, including mRNAs, microRNAs, long non-coding RNAs and others within a single cell is well-documented<sup>7</sup>. Yet, our understanding of the synergic or antagonistic interaction among these diverse m<sup>6</sup>A RNAs remains largely unexplored. In this regard, the development of sensitive and highly specific tools for profiling the m<sup>6</sup>A RNAs has emerged as a central and transformative focus in the realm of research efforts, holding tremendous potential for advancing our understanding of these intricate molecular networks.

Currently, commercialization methods for m<sup>6</sup>A RNA detection are mainly divided into three classes: overall level detection (e.g., liquid chromatography)<sup>8,9</sup>, high-throughput sequencing (e.g., methylated

<sup>1</sup>Shanghai Tenth People’s Hospital of Tongji University, Shanghai, PR China. <sup>2</sup>Department of Clinical Laboratory Medicine, Shanghai Children’s Medical Center, Shanghai Jiao Tong University School of Medicine, Shanghai, PR China. <sup>3</sup>Shanghai Pudong New Area People’s Hospital, Shanghai, PR China. <sup>4</sup>These authors contributed equally: Dongsheng Mao, Xiaochen Tang. ✉e-mail: [wenxingli@163.com](mailto:wenxingli@163.com); [panqihui\\_med@163.com](mailto:panqihui_med@163.com); [urodrshenbing@shsmu.edu.cn](mailto:urodrshenbing@shsmu.edu.cn); [xiaolizhu@tongji.edu.cn](mailto:xiaolizhu@tongji.edu.cn)

RNA immunoprecipitation sequencing, MeRIP-seq<sup>10,11</sup>, and modification level detection for specific fragments or sites of genes (e.g., MazF-qPCR)<sup>12</sup>. All these methods were non in-situ analysis, and they were either too complicated or lack of capacity in single molecule resolution and quantitative analysis<sup>13</sup>. Consequently, they result in the loss of critical spatial localization information, hinder the study of cellular heterogeneity, and incur high costs. In the context of precision medicine and precision biology, there is a pressing demand for novel analytical techniques capable of providing single-cell resolution and spatial information, with the ability to overcome the aforementioned obstacles.

Although existing methods for single RNA m<sup>6</sup>A analysis, in situ signal amplification, and multiplexed RNA detection have laid a solid foundation for the innovative design of multiplexed RNA m<sup>6</sup>A analysis systems<sup>14–18</sup>, achieving multiplexed, spatially resolved imaging of single-cell RNA m<sup>6</sup>A has remained a challenge in simultaneously addressing the following critical aspects: (1) High specificity: Given that this is a non-sequencing of omics study, imaging probes must exhibit exceptional targeting ability and specificity<sup>19</sup>. (2) Single molecule resolution: Since RNA imaging yields a single spot, signal amplification is required for clear observation<sup>20</sup>. (3) Multiplexed, spatially resolved analysis: In situ, multiplexing analysis of m<sup>6</sup>A RNAs holds great promise for unraveling the intricate interrelationships among them and for dissecting the nuances of single-cell heterogeneity<sup>21</sup>. For instance, Ren et al. proposed a RNA m<sup>6</sup>A-specific in situ hybridization-mediated proximity ligation assay (m<sup>6</sup>AISH-PLA) for cellular imaging of m<sup>6</sup>A RNA, enabling the identification of m<sup>6</sup>A modifications at specific locations in RNAs and the imaging of m<sup>6</sup>A RNAs with single-cell and single-molecule resolution<sup>14</sup>. Nonetheless, this approach still leaves room for improvement in terms of multiplexed detection and amplification method.

To achieve multiplexed, spatially resolved imaging of single-cell RNA m<sup>6</sup>A, we have developed a novel technique named PROximity

Exchange-assisted Encoding of Multichrome (PREEM). PREEM seamlessly integrates specific targeting through “AND” Boolean logic recognition and single-molecule resolution via the “CAD-HCR” amplification system, enabling the in-situ imaging of multiple m<sup>6</sup>A RNAs at the single-cell level<sup>22</sup>. Similar with recently developed “CAD-HCR” system, PREEM harnesses a sequence database designed through computer-aided methods to create customizable probes. Significantly, PREEM enables the initiation of an in situ two-bit multi-chrome hybridization chain reaction (HCR) through “AND” Boolean logic-mediated proximity exchange, revealing the spatial patterns of no fewer than 12 m<sup>6</sup>A RNAs using only 3 imaging channels. By employing PREEM, we have achieved quantitative and subcellular spatial distribution measurements of specific m<sup>6</sup>A RNAs, unveiling how m<sup>6</sup>A RNA patterns change in response to various biochemical regulation and drug stimulation. Our findings revealed that m<sup>6</sup>A RNAs exhibits an aggregation tendency in cellular localization, either within or outside the nucleus, and that the abundance changes of different m<sup>6</sup>A RNAs are not synchronized. Overall, PREEM represents a significant advancement in DNA self-assembly-based precise fluorescent encoding and high-throughput, reversible RNA m<sup>6</sup>A analysis technologies, enriching the toolbox for epigenetic research and clinical applications. The precise quantification and spatial location analysis of multiple m<sup>6</sup>A RNAs in single cells enabled by PREEM facilitate the exploration of how m<sup>6</sup>A RNAs expression regulation impacts the spatial and functional organization of cells.

## Results

### Design of PREEM for m<sup>6</sup>A RNA detection

PREEM was constructed via the following sequential processes to enable the detection of m<sup>6</sup>A RNAs within single cell (Fig. 1a). The core of PREEM involves a proximity exchange reaction utilizing proximity hairpin probe (PH1 and PH2) and proximity initiation probe (PI). PH1 contains proximity exchange and m<sup>6</sup>A antibody crosslinking regions,

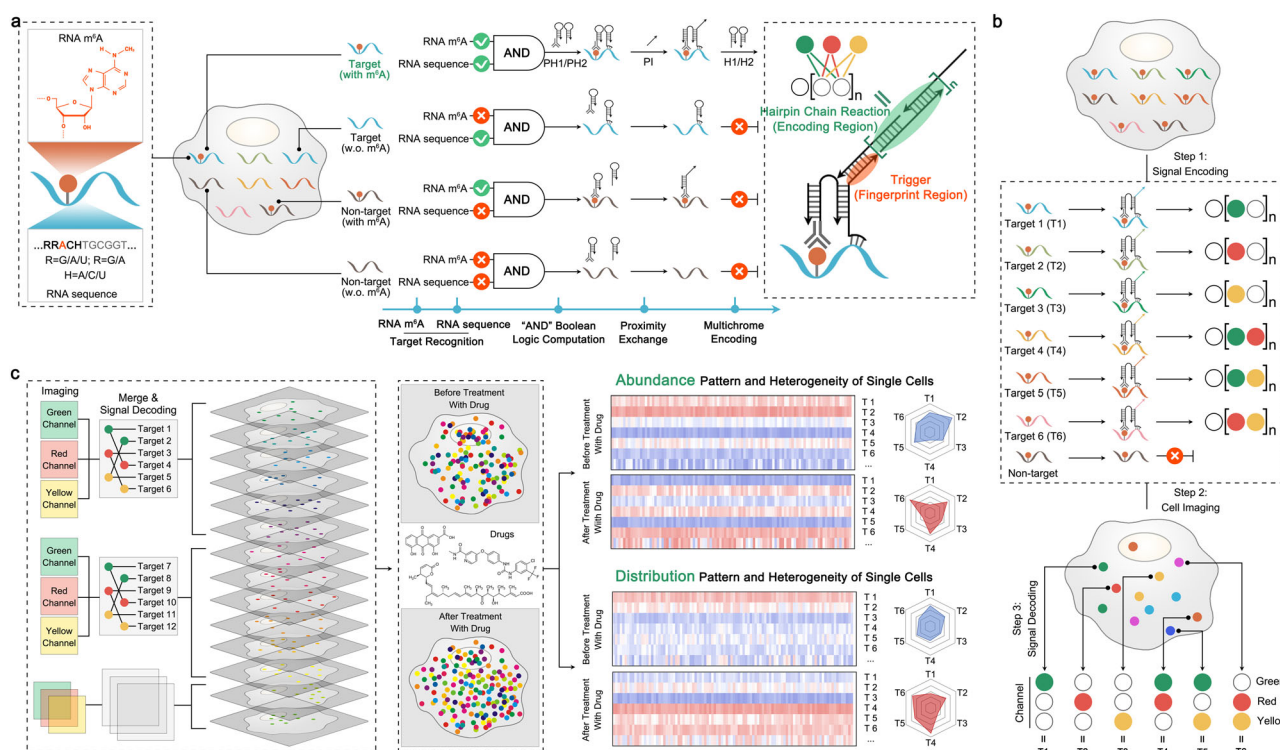


**Fig. 1 | PREEM for m<sup>6</sup>A RNA detection at the single-molecule resolution level in single-cells. a** Schematic illustration of different DNA elements in PREEM for “AND” Boolean logic computation and multichrome encoding. **b** Workflow of PREEM for

multiplexed m<sup>6</sup>A RNAs analysis. **c** Schematic illustration of multiplexed imaging for single-cell RNA epigenetic modifications with reversible PREEM-based cyclic imaging, enabling abundance, distribution patterns, and heterogeneity analysis of single cells.

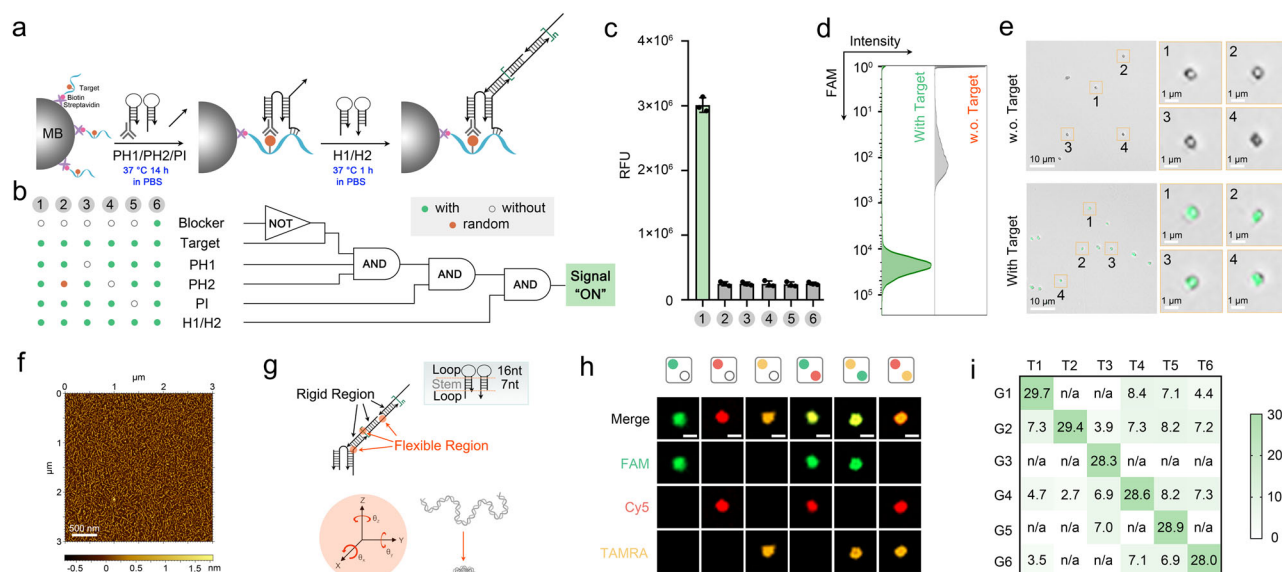


**Fig. 2 | Characterization of the feasibility of PREEM for m<sup>6</sup>A detection in vitro.**

**a** Schematic illustration of MMB-based PREEM for the detection of m<sup>6</sup>A RNA. **b** Schematic illustration of “AND” Boolean logic computation within PREEM. **c** Fluorescence signal generated by different PREEM systems with different elements. **d** Flow cytometry analysis and **e** confocal laser scanning microscopy images of PREEM system from 3 independent experiments, comparing scenarios with or without m<sup>6</sup>A modification. Scale bars: 10 μm. **f** Morphology of PREEM assemblies characterized by atomic force microscopy from 3 independent experiments. Scale bars: 500 nm. **g** Schematic illustration of the flexible structure of PREEM

assemblies. **h** Fluorescence microscopy imaging results of PREEM with two-bit, three-fluorophore system from 3 independent experiments. Scale bars: 1 μm. **i** Comparison of the thermal stability between trigger and hairpins in different groups. Data were obtained from NUPACK under the following parameters. Nucleic acid type: DNA; Temperature: 37 °C; Concentration: 1 μM; DNA energy parameters: SantaLucia 1998; Concentration of Na<sup>+</sup>: 50 mM; Concentration of Mg<sup>2+</sup>: 10 mM; Dangle treatment: Some. All values are negative. Data are presented as mean values ± s.d. Error bars represent the standard deviation of three independent experiments. Source data are provided as a Source Data file.

while PH2 contains regions for proximity exchange, fingerprint (Trigger) and target recognition. PI is used to trigger PH1 and cascade PH2 to undergo proximity exchange reaction, exposing programmable fingerprint region (Supplementary Fig. 1). Subsequently, the fingerprint region acts as primer for initiating HCR-based multichrome encoding. Notably, PH1 and PH2 form a proximity dependent “AND” Boolean logic computation, as they can bispecifically recognize both the RNA m<sup>6</sup>A modification and target RNA sequence. Moreover, PI controls the initiation or blockage of HCR-based multichrome encoding, thus minimizing nonspecific signal output. Consequently, this system yields fluorescence output only in the presence of both the target RNA sequences and m<sup>6</sup>A modifications. In cases where any input signal is missing or differs, HCR output cannot be initiated.

The workflow of PREEM is illustrated in Fig. 1b, involving three steps: signal encoding, cell imaging, and signal decoding. In detail, after efficient cellular targeting with PH1 (containing m<sup>6</sup>A antibody) and PH2 (containing target RNA recognition region), proximity exchange reaction will occur on target m<sup>6</sup>A site, further trigger in situ HCR-based multichrome encoding. It can be further imaged under multi-channel fluorescence microscope, and be analyzed through signal decoding. Firstly, for programmable assembly on HCR amplicons to form the multichrome encoding, HCR system (H1 and H2) are designed based previous database<sup>22</sup>. By altering fluorophores on H1 and H2, a variety of signal encoding combinations can be formed according to permutation. For example, with two-bit encoding and “n” kinds of fluorophores, (C1 n+ C2 n) combinations can be generated. The HCR amplicons can be visualized as bright spots with different distinct signal encoding combinations, enabling the identification of specific m<sup>6</sup>A RNAs. Technically speaking, the multiplexing capacity of PREEM for single detection can be expanded by increasing the number of fluorescence channels (number of fluorophores) and encoding bits (number of HCR elements). Here, we have enhanced the capacity for multiplexed detection of m<sup>6</sup>A RNA targets by expanding the number of targets through reversible PREEM-based cyclic imaging (Fig. 1c).

PREEM can provide expression level and localization information of target m<sup>6</sup>A RNAs with single-molecule resolution, advantageous to acquiring cell-to-cell variations and revealing the subcellular locations of target m<sup>6</sup>A RNAs in single cells.

### Characterization of the feasibility of PREEM in vitro

Firstly, to demonstrate the feasibility of PREEM for m<sup>6</sup>A RNA detection vividly, we employed a magnetic microbead (MMB)-based PREEM system to detect a synthetic target m<sup>6</sup>A ACTB RNA fragment (Supplementary Table 1). Biotinylated target was immobilized on streptavidin-coated MMB, and two hairpin probes (H1 and H2) were labeled with FAM. Hence, the generation of fluorescent signal by the products of HCR on MMB will provide intuitive evidence supporting the feasibility of PREEM (Fig. 2a). Considering that the distance between two proximity hairpin probes (PH1 and PH2) would profoundly influence reaction efficiency, we validated the influence of the distance between PH2 and the m<sup>6</sup>A site on proximity exchange reaction (Supplementary Fig. 2). Results indicate that the fluorescent signal reached a maximum when the distance of PH2 from the m<sup>6</sup>A site was 15 nt (Supplementary Fig. 2). Therefore, we selected a 15 nt distance from the m<sup>6</sup>A site for the hybridization of PH2 with the target. It could be inferred that too short distance might make it difficult for antibody binding due to steric hindrance, while too long distance was likely to prevent successful proximity exchange reaction triggered by PI. Furthermore, we optimized the reaction conditions including the time for PI hybridization and HCR (Supplementary Fig. 3). The optimal times for PI hybridization and HCR were determined about 60 min. We also optimized the concentration of each component of the PREEM system. Due to the one-to-one reaction of each probe in the reaction, the optimized concentration of probes was basically similar, about 500 nM (Supplementary Fig. 4a, b). For HCR hairpins, the higher the concentration, the stronger the output signal (Supplementary Fig. 4c). Therefore, considering factors such as signal amplification and actual fluorescence imaging intensity, we adopted a concentration of 500 nM



for HCR probes. On the other hand, due to the fact that overnight processing is usually required for antibody incubation (PH1-tagged antibody binding) and nucleic acid target hybridization (PH2 hybridization), we compared different experiment processes to shorten reaction time and optimize the overall reaction time. As shown in Supplementary Fig. 4d, e, compared to way 1, which involved first incubating the antibody and then hybridizing the probes, the process of way 2 shortened from 30 to 15 h, saving almost half of the time (50%). And, the results achieved by both ways were similar, so we adopted way 2 for subsequent experiments to further shorten the overall reaction time.

To validate the accuracy and specificity of PREEM for identifying RNA m<sup>6</sup>A modifications at specific locations within RNA, we designed a series of control experiments based on “AND” Boolean logic function (Fig. 2b), in which involves three fundamental reactions including bispecific recognition, proximity exchange, and fluorescence encoding. On the basis of the “AND” Boolean logic gate mentioned above, we constructed a logical “NOT” feeds into a logical “AND”, which the upstream “NOT” gate prevented the hybridization between PH2 and target with the addition of Blocker sequence (complementary with the target). As shown in Fig. 2c, in comparison to the fluorescence signal generated with the whole PREEM system with targeting m<sup>6</sup>A RNA (Target), there was a sharply decreased fluorescence signal when with no corresponding probes (PH1, PH2 or PI) or when PH2 contained a random sequence. Similarly, the fluorescence signal still remained low when the target hybridized with complementary sequence (Blocker). This indicated that the integrity of PREEM system is essential to the accurate identification of the target and the precise identification of m<sup>6</sup>A modification. Moreover, the fluorescence signal in Target group was significantly higher than that of Control group (without m<sup>6</sup>A modification), demonstrating that PREEM could distinguish m<sup>6</sup>A from unmodified adenosine (A). Flow cytometry and confocal fluorescence microscopy imaging results further confirmed the robust performance of PREEM, regardless of the presence or absence of m<sup>6</sup>A modification (Fig. 2d, e). Through setting up three m<sup>6</sup>A RNA target mimics as the model, the interaction capacity between probes was further investigated. The orthogonality results in MMB revealed the reaction efficiency and specificity of the PREEM system on different targets, which the correct assembly of PREEM probes could be triggered only in the presence of the corresponding target, otherwise the proximity exchange reaction could not proceed (Supplementary Fig. 5). Additionally, we characterized the morphology of PREEM products using atomic force microscopy (AFM), which exhibited an irregular curved structure consistent with assembly theory (Fig. 2f). More importantly, since the PREEM products contain flexible region, it was expected to be able to converge into clusters, facilitating single molecule detection (Fig. 2g). To sum up, these findings provided evidence for the feasibility and efficiency of constructing PREEM with Boolean logic gate. They demonstrate the critical importance of the design of each element in PREEM and highlight that the operation of PREEM was highly dependent on m<sup>6</sup>A modification, ensuring minimal background interference, thereby allowing for precise control of logic functions.

We then determined the analytical sensitivity of the approach, and a detection experiment was performed using synthetic m<sup>6</sup>A RNAs with different concentrations ranging from 10<sup>-13</sup> to 10<sup>-5</sup> M (Supplementary Fig. 6). There was a strong dose-dependent fluorescence signal and the lowest detection limit around 10<sup>-12</sup> M. In comparison, the fluorescence concentration (buffer with fluorescent nucleic acids) detected by using the same instrument was about 10<sup>-10</sup> M (Supplementary Fig. 6c), and through our method, the signal could be amplified by ~100 times, greatly increasing the sensitivity of detection. Thus, this is a highly sensitive assay which can be used for the quantification of m<sup>6</sup>A modification at specific location in RNAs.

Lastly, we characterized the encoding capacity of PREEM with a two-bit, three-fluorophore system on a model interface represented by

MMB, which could encode 6 unique barcodes. To avoid the potential interference from spectral overlap, we selected three distinct fluorophores: FAM (Green, G), TAMRA (Yellow, Y), and Cy5 (Red, R), and the fluorescence imaging results were highly consistent with the design theory (Fig. 2h). Subsequently, the orthogonal reactivity of signal encoding was subsequently validated, which is a necessary prerequisite for achieving multiplexed target detection. To match the above signal encoding principles, we established 6 groups of orthogonal HCR (Supplementary Table 1). PAGE analysis was adopted to study the assembly of HCR. In the presence of trigger sequence (the second lane of each group), H1 and H2 could form dispersed amplified products, while there was a clear monomer band in the absence of trigger sequence (Supplementary Fig. 7a). We further analyzed the orthogonality of each group to evaluate the feasibility of multiple analysis of m<sup>6</sup>A RNAs. Results confirmed that only the trigger sequence of the corresponding group could initiate HCR, while others were ineffective (Supplementary Fig. 7b–d). Theoretical analysis and MMB experiments also showed that all groups of PREEM exhibited proper functionality and high degree of orthogonality (Fig. 2i and Supplementary Fig. 8). These results confirmed the excellent performance of our PREEM system in vitro, which laid a theoretical foundation for multiplexed analysis of m<sup>6</sup>A RNAs within single cell. The design of nucleic acid sequence simulation based on MMB model not only laid the foundation for assessing the feasibility of PREEM but also enabled its various potential applications. By modifying relevant elements of PREEM, we can adapt it for visualizing other RNA modifications and analyzing various intermolecular interactions.

### PREEM for in situ imaging of m<sup>6</sup>A RNA

In mammalian cells, the m<sup>6</sup>A modification is maintained by the cooperation of a set of enzymes, constituting a dynamic regulatory process<sup>23,24</sup>. To investigate whether the PREEM system can be used for in situ m<sup>6</sup>A RNA imaging, PH2 probe was designed to target the m<sup>6</sup>A at the 1216th site of the cell-derived human endogenous actin beta (ACTB) mRNA. The ACTB gene is a kind of house-keeping gene, which can be stably expressed and is necessary for maintaining the basic life activities of cells<sup>25</sup>. m<sup>6</sup>A modification of ACTB is common in various cells and is related to selective translation and cell stability<sup>26</sup>. To prepare for in situ m<sup>6</sup>A RNA imaging, PH1 tagged-m<sup>6</sup>A antibody was synthesized using the principle of click chemistry (DBCO and NHS-PEG<sub>4</sub>-Azide). PAGE analysis was performed to confirm the formation of the PH1 tagged-m<sup>6</sup>A antibody complex. As shown in Supplementary Fig. 9, compared to the native m<sup>6</sup>A antibody, PH1 tagged-m<sup>6</sup>A antibody complex exhibited a tailing phenomenon and a slower migration rate, indicating successful crosslinking between the antibody and PH1 probes. Then, PH1 tagged-m<sup>6</sup>A antibody was adopted for conventional immunofluorescence imaging to detect the functionality and immunogenicity retention of primary antibody. Results showed that the modified m<sup>6</sup>A antibody maintained great functionality and immunogenicity with high specificity, and can be used for the following experiments (Supplementary Fig. 10). We further optimized the reaction time for PI hybridization and HCR in the context of in situ m<sup>6</sup>A imaging within single cells (Supplementary Fig. 11). Different from in vitro optimization results, the reaction time required for cell imaging had been prolonged, which might be due to the complex cellular environment. Taking conventional immunofluorescence (IF) as control, bright fluorescent spots of ACTB RNA-m<sup>6</sup>A were observed with high specificity in the cells by PREEM (Fig. 3a), indicating that PREEM can realize specific detection of m<sup>6</sup>A RNA at the single molecular level. In contrast, fluorescence showed dispersion distribution without specificity in conventional IF. While in fluorescence in situ hybridization (FISH) for ACTB mRNA imaging, there were significantly more fluorescent spots than that in PREEM, further confirming the specificity of PREEM for m<sup>6</sup>A modification imaging (Fig. 3a). Through connected component analysis, we demonstrated the specificity of PREEM

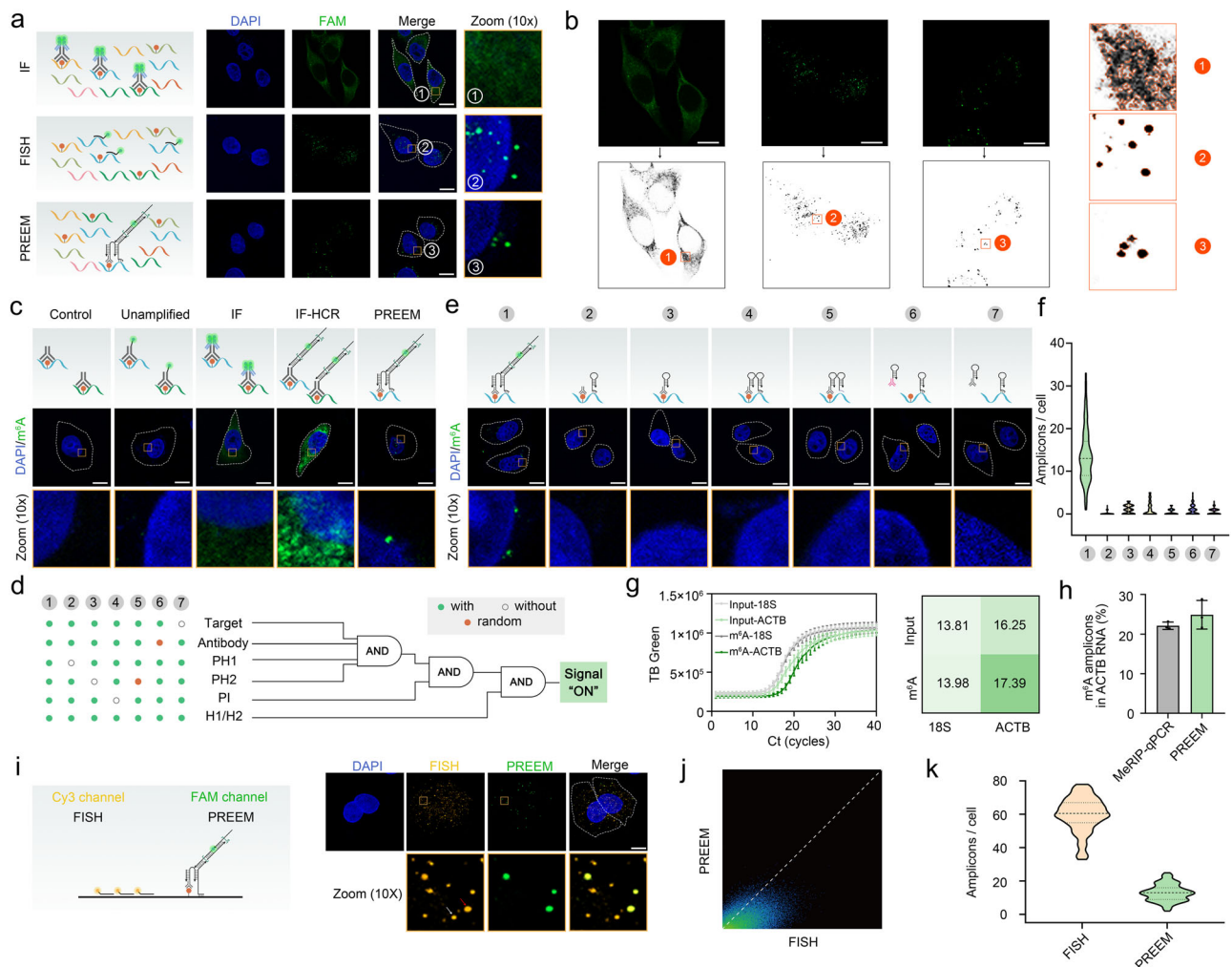


**Fig. 3 | Visualization of m<sup>6</sup>A RNAs in HeLa cells using PREEM.** **a** Overall m<sup>6</sup>A level visualized by Immunofluorescence (IF), mRNA level by fluorescence in situ hybridization (FISH) and ACTB RNA 1216-m<sup>6</sup>A level by PREEM in HeLa cells from 3 independent experiments. Scale bars: 10  $\mu$ m. **b** Connected domain analysis of fluorescence signal distribution from 3 independent experiments. Scale bars: 10  $\mu$ m. **c** Confocal laser scanning microscope images of m<sup>6</sup>A level in HeLa cells by using different methods, including unamplified, IF, IF-HCR, and PREEM from 3 independent experiments. Scale bars: 10  $\mu$ m. **d** Schematic illustration of different DNA elements in PREEM for logic computation in the detection of m<sup>6</sup>A RNA at the single cell level. **e** Representative cell images of ACTB RNA 1216-m<sup>6</sup>A in HeLa cells generated by different PREEM systems with different elements. Scale bars: 10  $\mu$ m. **f** Violin chart of amplicons counted for each sample in single cells ( $N=100$ ).  $N$

represents the number of single cells for each sample. **g** Real-time fluorescence curves in MeRIP-qPCR analysis. **h** Quantification of m<sup>6</sup>A amplicons in ACTB RNA by PREEM and MeRIP-qPCR. **i** Schematic illustration of m<sup>6</sup>A RNA imaged by PREEM (FAM channel) and RNA by FISH (Cy3 channel). Right section, fluorescence images of ACTB RNA and ACTB RNA 1216-m<sup>6</sup>A in single cells ( $N=100$ ).  $N$  represents the number of single cells. Scale bars: 10  $\mu$ m. **j** Colocalization analysis of ACTB mRNA and m<sup>6</sup>A amplicons. **k** Violin chart of amplicons counted for ACTB mRNA and m<sup>6</sup>A in single cells ( $N=100$ ).  $N$  represents the number of single cells for each sample. Data are presented as mean values  $\pm$  s.d. Error bars represent the standard deviation of three independent experiments. Source data are provided as a Source Data file.

imaging and the uniformity of spot distribution (Fig. 3b). In parallel, to evaluate the signal amplification capability of PREEM, we performed five sets of m<sup>6</sup>A modification staining in cultured cells and analyzed the fluorescence signal (Fig. 3c). There was a weak signal in the unamplified group, and the PREEM system significantly enhanced the fluorescence, surpassing the signal achieved by the secondary antibodies in conventional IF. Compared to conventional IF, HCR in IF displayed stronger signals. At the same time, under the same HCR conditions, PREEM exhibited specific imaging targeting specific m<sup>6</sup>A mRNA (manifested as granular distribution), whereas HCR in IF only targeted the overall m<sup>6</sup>A level in cells (manifested as diffuse distribution).

To confirm the essential role of each element in m<sup>6</sup>A RNA imaging using the PREEM system, a series of control experiments based on “AND” Boolean logic function was conducted, similar to in vitro experiments (Fig. 3d). Figure 3e presents that bright spots in the target group could be obviously identified from the background, but almost

no bright spots were observed when missing the key proximity probes. The spot count of single cells was used for the quantitative analysis, and we counted the number of m<sup>6</sup>A amplicons in 100 single cells. The number of amplicons in each cell was a set of data, corresponding to 100 sets of data, and the quantification data showed that the amplicon number in target group (13.74/cell) was significantly higher than in other groups, including no PH1 (0.13/cell), no PH2 (1.09/cell), and no PI (1.17/cell) (Fig. 3f and Supplementary Fig. 12). This confirmed that the bright spots representing m<sup>6</sup>A RNA at the single molecule level relied on the binding of proximity probes. Moreover, there was only a rare fluorescence signal when using PH2 probe with random sequence (0.48/cell) or IgG Fc - PH1 (0.91/cell), demonstrating the high sequence specificity of the PREEM system for the m<sup>6</sup>A RNA identification. In addition, we selected the region of ACTB without m<sup>6</sup>A modification and designed corresponding probes. As shown in Fig. 3e, the absence of m<sup>6</sup>A methylation in ACTB evoked no signal. Statistical analysis

confirmed that the fluorescence amplicons from the target m<sup>6</sup>A mRNA (13.74/cell) were markedly different from that of the negative control (0.57/cell) (Fig. 3f), further corroborating the high specificity of PREEM.

To illustrate the accuracy of the approach, we extracted the total RNA in HeLa cells and performed MeRIP-qPCR to analyze the m<sup>6</sup>A level of ACTB. The statistical results displayed that the proportion of m<sup>6</sup>A RNA obtained by PREEM was  $24.89 \pm 3.62\%$ , and the proportion of m<sup>6</sup>A RNA obtained by MeRIP-qPCR was  $22.11 \pm 0.94\%$  (Fig. 3g, h). These results were basically consistent and in accordance with the previous report<sup>27</sup>. Notably, PREEM could more effectively detect single cell heterogeneity with higher bar values, while MeRIP-qPCR results reflected experimental system or instrument errors with lower bar values. On the other hand, we performed RNA-FISH with PREEM using super-resolution microscopy, and the colocalization experiment showed that the m<sup>6</sup>A signal was overlapped with the RNA signal, indicating that the detected bright spots of m<sup>6</sup>A originated from the m<sup>6</sup>A modification in ACTB RNA rather than nonspecific background signals (Fig. 3i–k). Overall, these results demonstrated the suitability of PREEM for in situ labeling of m<sup>6</sup>A RNA in cells, offering single molecule resolution, high specificity, and high accuracy.

### Response of PREEM to changes in m<sup>6</sup>A RNA levels

The complex dynamics of m<sup>6</sup>A RNA methylation play a vital role in the occurrence and development of various diseases<sup>28,29</sup>. Therefore, in addition to clarifying the target RNA m<sup>6</sup>A level in cells, the sensitivity of PREEM to the change of RNA m<sup>6</sup>A levels is of paramount importance. We applied PREEM to investigate the dynamics of m<sup>6</sup>A RNA methylation response to different treatments. To simulate these dynamics and elevate RNA m<sup>6</sup>A levels, we treated HeLa cells with heat shock (HS), a cellular protective mechanism that can increase RNA methylation levels (Fig. 4a)<sup>30</sup>. This increase in RNA methylation was confirmed by immunostaining, which revealed an overall elevation of the m<sup>6</sup>A level in cells (Supplementary Fig. 13). By the PREEM approach, we observed an elevation in the number of ACTB RNA 1216-m<sup>6</sup>A (from 11.44 to 28.32 per cell) after the HS treatment (Fig. 4b, c). The m<sup>6</sup>A modified ratio of ACTB at the 1216th site also exhibited an increase, rising from 22.85% to 33.46%, representing a 1.46-fold improvement (Fig. 4d). The overall m<sup>6</sup>A level detected by commercial kit and the m<sup>6</sup>A level of ACTB RNA quantified by MeRIP-qPCR were both verified the accuracy of PREEM and the consistency of the results (Fig. 4e, f). The increase in m<sup>6</sup>A levels might result from the protective mechanism under stress conditions, which protected ACTB RNA from demethylation<sup>31</sup>. Also, the parallel cellular sampling provides an opportunity to study the heterogeneous regulation within a large population of cells. The distribution of amplicon frequency and statistical analysis of m<sup>6</sup>A proportion in ACTB RNA 1216-m<sup>6</sup>A showed an obvious cell-to-cell variability, reflecting a nonuniform epigenetic response within the same cell population.

Methyltransferase-like 3 (METTL3) possesses an active methyltransferase domain to catalyze the conversion of adenosine (A) to m<sup>6</sup>A, and the depletion of METTL3 may significantly impact the methylation levels and disrupt multiple signaling pathways, contributing to the occurrence and development of diseases<sup>32,33</sup>. Hence, in another model of a METTL3-knockdown-induced cellular response, the down-regulated m<sup>6</sup>A modification can also be captured by PREEM (Fig. 4g and Supplementary Fig. 14). As expected, the overall m<sup>6</sup>A level in cells was slightly lower, although not as obvious as the increase caused by HS (Supplementary Fig. 15). Similarly, we observed the fluorescence change of ACTB RNA 1216-m<sup>6</sup>A in single cells, and further analyzed amplicons upon METTL3 knockdown (Fig. 4h, i). There was a slight decrease (from 12.87 to 8.96 per cell) in the number of m<sup>6</sup>A amplicons and the m<sup>6</sup>A modified ratio was also reduced from 21.13% to 12.33% (Fig. 4j). However, the difference in change was not greatly significant,

speculating that the role of METTL3 in m<sup>6</sup>A modification could be compensated by other enzymes for methyltransferase<sup>34</sup>. The results from overall m<sup>6</sup>A level and MeRIP-qPCR also confirmed that METTL3 knockdown did not yield a particularly sensitive cellular methylation response (Fig. 4k, l), which are aligned with the findings from the PREEM analysis.

Furthermore, we performed ACTB knockdown using the small interfering RNA (siRNA) system, and confirmed the knockdown efficiency via RT-qPCR assay (Fig. 4m and Supplementary Fig. 16). As the target was missing, it is speculated that the methylation level of ACTB alone would decrease significantly, but would not obviously affect the overall m<sup>6</sup>A level. As expected, the fluorescence signal of overall m<sup>6</sup>A by IF basically unchanged before and after ACTB knockdown (Supplementary Fig. 17), while the amplicons of ACTB RNA 1216-m<sup>6</sup>A decreased to 2.23/cell (Fig. 4n, o), demonstrating the specificity of the approach again. More specifically, it was emphasized that even though the overall m<sup>6</sup>A alteration was not obvious, our approach could be used for identification and differentiation of site-specific m<sup>6</sup>A RNA yet (Fig. 4p–r).

Consequently, comparing to existing methods, PREEM can not only provide the in situ imaging and precise quantification of m<sup>6</sup>A modification, but also pick up information about modification extent and cell heterogeneity, further demonstrating the flexibility and versatility of PREEM for analyzing m<sup>6</sup>A modification.

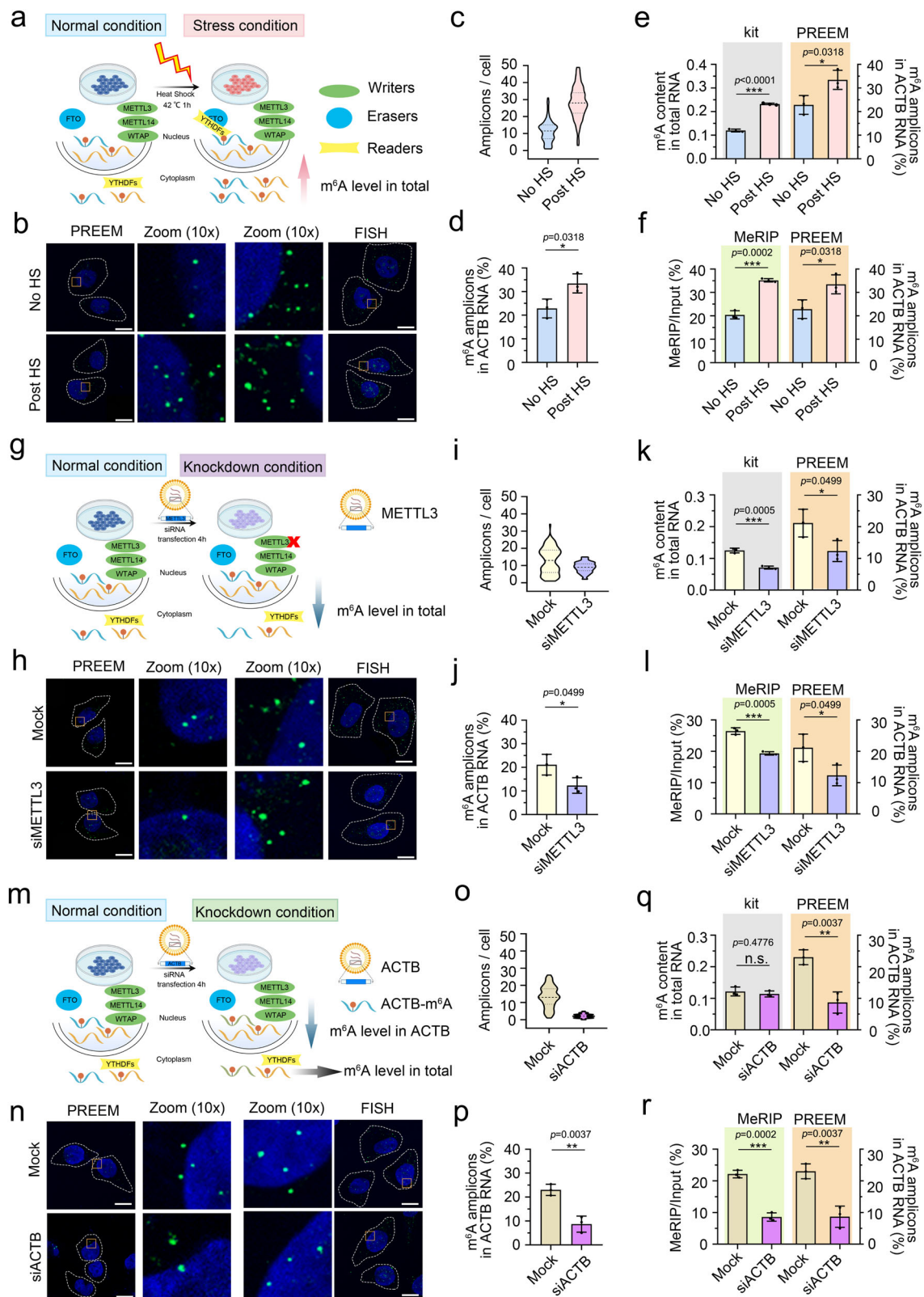
### PREEM for multiple m<sup>6</sup>A RNA imaging

The expression of RNA is regulated by complex regulatory networks, and in the epigenetic regulation related to m<sup>6</sup>A modification, different types of m<sup>6</sup>A RNAs could work synergically or oppositely to achieve a delicate balanced<sup>35,36</sup>. However, there are currently limited methods available for in situ detection of multiple m<sup>6</sup>A RNAs. Toward this goal, we investigated the universality of PREEM and further focused on its application in multiplexed imaging to achieve simultaneously detection of various m<sup>6</sup>A RNAs at the single-molecule level.

To show the universality of PREEM for detecting m<sup>6</sup>A RNA, we examined it from two dimensions: different cell types and RNA species. As shown in Fig. 5a, m<sup>6</sup>A amplicons of CTNNB1 in human hepatoblastoma cells (HepG2) and MZF1 in lung cancer cells (A549) were chosen to be analyzed and the average copy number was 2.63 and 7.07 per cell, respectively. Furthermore, we have successfully applied PREEM to image the specific m<sup>6</sup>A RNA in various mRNA and long non-coding RNA (lncRNA) (Fig. 5b). On the basis of RNA level obtained using FISH, the calculated m<sup>6</sup>A occupancies were in good accordance with previous report<sup>27</sup> (Supplementary Fig. 18 and Supplementary Table 2). It is worth noting that the expression levels of different RNA species were remained distinct, reflecting the importance of simultaneous analysis for providing a more comprehensive information of m<sup>6</sup>A modification within single cells.

Accordingly, to endow PREEM with the multiplexing capacity, the HCR amplicons were encoded by the permutation of fluorophores. We chose three fluorophores (FAM, Cy5, and TAMRA) as instance to encode six m<sup>6</sup>A RNAs in HeLa cells, and the encoding principle was already validated on magnetic beads (Fig. 2h). We conducted six group imaging experiments in cells, and observed excellent orthogonality for in situ fluorescence imaging (Supplementary Fig. 19). In these experiments, only the orthogonal PREEM system successfully triggered the corresponding HCR for fluorescence signal output, suggesting that the assemblies of HCR barcodes can be programmed for multiplexed fluorescence imaging. As mentioned above, PREEM exhibited practicable detection efficiency and high specificity. The excellent performance would enable its application in multiplexed imaging. We then explored the capabilities of PREEM for multiplexed imaging of m<sup>6</sup>A RNAs in HeLa cells. For a proof of principle experiment, PREEM was performed in the fixed cells. It could be seen in Fig. 5c that the amplicons of different m<sup>6</sup>A RNAs were marked with various pseudo





colors. Plotting the channels distribution of amplicons demonstrated that six kinds of amplicons targeting different m<sup>6</sup>A RNAs can be effectively identified, indicating that the multiple target m<sup>6</sup>A RNAs could be identified and encoded by PREEM. Subsequently, the tissue sections were detected by PREEM. Three m<sup>6</sup>A RNAs (ACTB, BSG, TPT1) in mouse liver tissue sections were selected as target models and analyzed here. It could be seen in Supplementary Fig. 20 that the

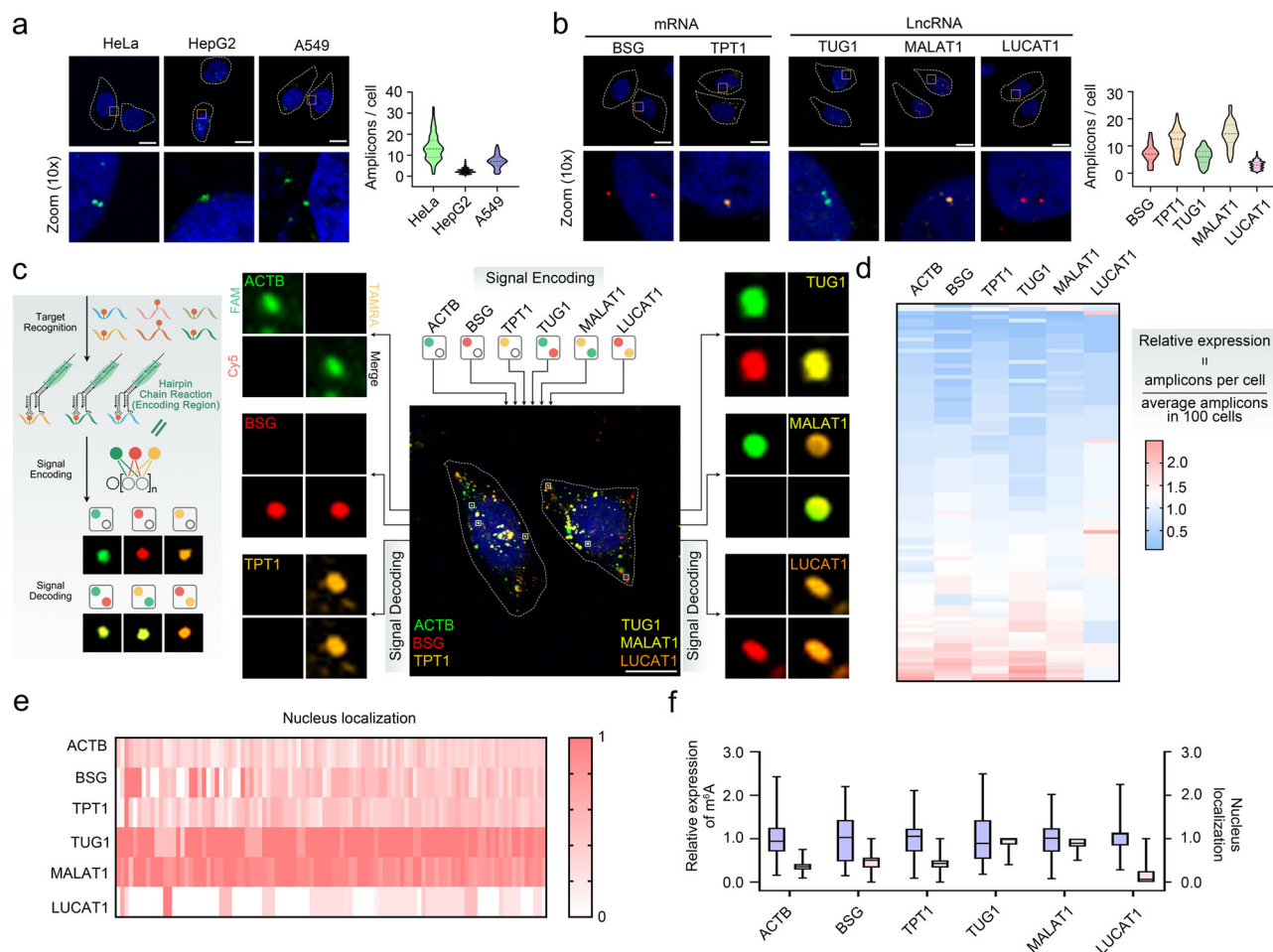
positive fluorescence signals distributed around the liver tissue, suggesting that our method still offered practicable detection efficiency and high specificity.

We further obtained variability in the expression level of each measured m<sup>6</sup>A RNA in single HeLa cells through the ratio of m<sup>6</sup>A amplicons per cell to the average value, revealing the significant cell-to-cell variation in expression for these m<sup>6</sup>A RNAs (Fig. 5d). In brief, the

**Fig. 4 | Dynamic changes of m<sup>6</sup>A RNAs monitored by PREEM in HeLa cells.**

**a** Schematic illustration of heat shock treatment to increase the m<sup>6</sup>A level in cells. **b** Fluorescence images of ACTB RNA 1216-m<sup>6</sup>A in single cells with HS treatment. Scale bars: 10  $\mu$ m. **c** Violin chart of amplicons counted in cells with HS treatment ( $N=100$ ).  $N$  represents the number of single cells for each sample. **d** Quantification of m<sup>6</sup>A amplicons in ACTB RNA by PREEM with HS treatment. **e** Relative m<sup>6</sup>A overall level in cells with HS treatment compared with PREEM. **f** Performance comparison between MeRIP-qPCR and PREEM to quantify the relative m<sup>6</sup>A level of ACTB with HS treatment. **g** Schematic illustration of METTL3 knockdown to decrease the m<sup>6</sup>A level in cells. **h** Fluorescence images of ACTB RNA 1216-m<sup>6</sup>A in single cells upon METTL3 knockdown. Scale bars: 10  $\mu$ m. **i** Violin chart of amplicons counted in cells upon METTL3 knockdown ( $N=100$ ).  $N$  represents the number of single cells for each sample. **j** Quantification of m<sup>6</sup>A amplicons in ACTB RNA by PREEM upon METTL3 knockdown. **k** Relative m<sup>6</sup>A overall level in cells upon METTL3 knockdown

compared with PREEM. **l** Performance comparison between MeRIP-qPCR and PREEM to quantify the relative m<sup>6</sup>A level of ACTB upon METTL3 knockdown. **m** Schematic illustration of ACTB knockdown to decrease the m<sup>6</sup>A level in cells. **n** Fluorescence images of ACTB RNA 1216-m<sup>6</sup>A in single cells upon ACTB knockdown. Scale bars: 10  $\mu$ m. **o** Violin chart of amplicons counted in cells upon ACTB knockdown ( $N=100$ ).  $N$  represents the number of single cells for each sample. **p** Quantification of m<sup>6</sup>A amplicons in ACTB RNA by PREEM upon ACTB knockdown. **q** Relative m<sup>6</sup>A overall level in cells upon ACTB knockdown compared with PREEM. **r** Performance comparison between MeRIP-qPCR and PREEM to quantify the relative m<sup>6</sup>A level of ACTB upon ACTB knockdown. \* $p < 0.05$ , \*\* $p < 0.01$ , \*\*\* $p < 0.001$ . Data are presented as mean values  $\pm$  s.d. Error bars represent the standard deviation of three independent experiments. Source data are provided as a Source Data file.

**Fig. 5 | Multiplexed m<sup>6</sup>A RNA imaging in single cells using PREEM.**

**a** Fluorescence images of ACTB m<sup>6</sup>A level in HeLa cells, CTNNB1 m<sup>6</sup>A level in HepG2 cells, and MZF1 m<sup>6</sup>A level in A549 cells visualized by PREEM. Scale bars: 10  $\mu$ m. Right section, violin chart of three m<sup>6</sup>A amplicons counted in single cells ( $N=100$ ).  $N$  represents the number of single cells for each sample. **b** Fluorescence images of BSG mRNA, TPT1 mRNA, TUG1 lncRNA, MALAT1 lncRNA, and LUCAT1 lncRNA m<sup>6</sup>A in single cells visualized by PREEM. Scale bars: 10  $\mu$ m. Right section, violin chart of five m<sup>6</sup>A amplicons counted in single cells ( $N=100$ ).  $N$  represents the number of single cells for each sample. **c** Fluorescence images for the spatial distribution of six

m<sup>6</sup>A RNAs in HeLa cells ( $N=100$ ).  $N$  represents the number of single cells. Scale bars: 10  $\mu$ m. **d** Heat map showing expression pattern of six m<sup>6</sup>A RNAs by analyzing the amplicons in cells by PREEM. **e** Heat map showing subcellular distribution of six m<sup>6</sup>A RNAs. All fluorescence measurements were normalized against expression level of the respective marker. **f** Quantification of average relative expression and nucleus localization for six m<sup>6</sup>A RNAs. The appearance of the box plots is through box and whiskers, and the whiskers are through min to max. Error bars represent the standard deviation of three independent experiments. Source data are provided as a Source Data file.

detected copy numbers of six m<sup>6</sup>A RNAs (ACTB, BSG, TPT1, TUG1, MALAT1, and LUCAT1) in single cells exhibited a broad range of diversity, in spite of highly parallel cellular sampling, further emphasizing the importance of single cell analysis. Notably, the m<sup>6</sup>A level of each RNA in a single cell maintained a certain level of consistency, that is, the change of m<sup>6</sup>A level across various RNAs were relatively

synchronized, possibly related to the overall m<sup>6</sup>A level. However, there was also special cases, for example, the m<sup>6</sup>A level of LUCAT1 in some cells was different from the other five RNA changes, indicating that the m<sup>6</sup>A level of LUCAT1 was not consistent with the overall m<sup>6</sup>A level. This highlighted the urgent need to analyze the m<sup>6</sup>A level of site-specific RNA rather than the overall m<sup>6</sup>A level.



What's more, subcellular localization of RNAs and their modifications may be related to various functionalities<sup>37,38</sup>. The sequencing technology cannot obtain the spatial information of RNAs in spite of high throughput. Nevertheless, by leveraging HCR barcoding and the in situ visualization capability of PREEM, we could examine the subcellular localization of m<sup>6</sup>A RNAs, mainly dividing into the cytoplasm and nucleus (Fig. 5e). The percentages of amplicons in nucleus were different according to RNA species, with three mRNAs (ACTB, BSG, TPT1) having 34.88%, 45.87%, and 41.64% of their amplicons in the nucleus, while 92.27% of TUG1 amplicons, 88.46% of MALAT1 amplicons, and 15.61% of LUCAT1 amplicons distributed in the nucleus (Fig. 5e). These RNAs were not uniformly distributed in cells, hinting that m<sup>6</sup>A methylation and spatial distribution of RNAs were functionally related (Fig. 5f). More systematic analysis of these single-cell m<sup>6</sup>A RNA expression levels and subcellular localization may allow the accurate representation of cellular states. PREEM could simultaneously investigate the copy number and localization of m<sup>6</sup>A RNAs, allowing us to reveal cellular heterogeneity and explore the intricate relationship between epitranscriptomic modification and cellular states.

### Exploring the impact of drug treatments on m<sup>6</sup>A RNA patterns with PREEM

With the rapid accumulation of research interest in m<sup>6</sup>A, its crucial roles in the regulations of disease development and drug response are gaining more and more attention. Altered m<sup>6</sup>A RNA patterns often related to tumor progress, yet the relationship between drug-induced changes in m<sup>6</sup>A RNA expression and localization to treatment in tumors remains elusive<sup>39,40</sup>. Based on the capability of PREEM in the detection of the expression and spatial distribution changes of m<sup>6</sup>A RNAs, we explored its application in visualizing m<sup>6</sup>A RNA pattern changes with different drug treatments. Here, we selected several common drugs based on the database 'M6AREG'<sup>41</sup>, and tried to study the correlation between changes in expression and localization profiles of m<sup>6</sup>A RNAs and drug treatment.

We first treated cells with each drug: rhein, meclofenamic acid (MA), doxorubicin (DOX), cisplatin (CDDP), sorafenib, and leptomycin B (LMB). Rhein and MA are reported to reversibly bind to the fat mass and obesity-associated (FTO) protein or AlkB dioxygenases, resulting in the formation of a complex. The complex prevents the recognition of m<sup>6</sup>A substrates inside cells, ultimately leading to an increase of cellular m<sup>6</sup>A RNAs<sup>42,43</sup>. However, the specific impact of Rhein and MA on intracellular localization changes have not yet been explored. DOX, CDDP and sorafenib are the commonly used chemotherapeutic agents, and can influence chemosensitivity via changes in m<sup>6</sup>A level<sup>44,45</sup>. LMB is a Streptomyces metabolite that inhibits the chromosomal region maintenance (CRM)1-mediated nuclear export of proteins in m<sup>6</sup>A-dependent pattern<sup>46,47</sup>. In HeLa cells, we optimized drug concentrations and treating times to ensure minimal impact on cell viability: rhein (100  $\mu$ M for 48 h), MA (50  $\mu$ M for 24 h), DOX (10  $\mu$ M for 24 h), CDDP (5  $\mu$ M for 24 h), sorafenib (4  $\mu$ M for 48 h), and LMB (20 nM for 24 h) (Supplementary Fig. 21). Firstly, we observed the overall m<sup>6</sup>A level with different drugs treatment through immunostaining (Supplementary Fig. 22), and further applied PREEM to characterize the expression level and nuclear distribution of specific m<sup>6</sup>A RNAs. Specifically, after exposure to LMB alone, six m<sup>6</sup>A RNAs (ACTB, BSG, TPT1, TUG1, MALAT1, and LUCAT1) exhibited varying degrees of changes in expression or localization (Fig. 6a–c). Using DMSO treatment as a control, we quantified the levels of these six RNA targets by RT-qPCR. Results indicate that five RNAs showed decreased expression except ACTB (Fig. 6d). Furthermore, we tried to evaluate the distribution of the aforementioned targets through nuclear plasma separation assay (Supplementary Fig. 23). As shown in Fig. 6e, almost each RNA showed increased nuclear distribution in LMB-treated cells, suggesting a critical role for LMB in the nuclear export of these m<sup>6</sup>A RNAs. However, the overall m<sup>6</sup>A RNA level showed almost unchanged, indicating that

the increase in nuclear levels was not caused by general transcription (Fig. 6f). We hypothesized that m<sup>6</sup>A RNA distributions were associated with chromosome region maintenance 1 (CRM1), which might impact the intracellular trafficking of m<sup>6</sup>A RNAs<sup>47</sup>. Similarly, we tested the effect of five other drugs on m<sup>6</sup>A RNAs through PREEM, further confirmed the accuracy of PREEM and the value of PREEM in revealing the relationship between drug treatment and changes in m<sup>6</sup>A RNA patterns (Supplementary Figs. 24–28). To more intuitively understanding the impact of drugs on m<sup>6</sup>A RNA patterns, we compared the expression and localization changes in m<sup>6</sup>A RNAs treated with different drugs (Fig. 6g, h). Generally speaking, while the changes in six m<sup>6</sup>A RNAs were relatively consistent under the same drug treatment, the magnitude of change varied. Of course, there were exceptions, such as LUCAT1 showing a downward expression trend under various drug treatments, and exhibiting different nuclear localization changes (increased nucleation/nuclear accumulation) from the other five m<sup>6</sup>A RNAs after sorafenib and MA exposure. This prompt that the changes in the overall level cannot reflect the changes in the individual level, and in the general context of the same trend of change, some could exhibit reverse changes. Taken together, our results demonstrated that PREEM could detect expression and distribution level of m<sup>6</sup>A RNAs in response to drug treatment, further confirming the value of visual detection.

In order to enhance the confidence in evaluating the applicability of the PREEM system, we performed m<sup>6</sup>A-seq analysis to obtain a transcriptome-wide m<sup>6</sup>A map before and after drug treatment to further assist in verifying the imaging results of PREEM (Supplementary Figs. 29–34). Global m<sup>6</sup>A methylome analysis revealed a similar pattern of m<sup>6</sup>A distribution before and after drug treatment. Our findings suggested that there was typical enrichment of m<sup>6</sup>A around the stop codon and coding sequence (CDS) (Supplementary Figs. 29a–34a). Besides, to determine if the m<sup>6</sup>A peaks had consensus sequence of RRACH (where RR Represents purine, A is m<sup>6</sup>A and H is a non-guanine base), *de-novo* motif analysis by using program Multiple Em for Motif Elicitation (MEME) were performed and we identified the consensus sequence "GGAC" among the significant peaks representing the common consensus in different groups, consistent with the previous use of database prediction for sequence design (Supplementary Figs. 29b–34b). Further to explore the relationship between m<sup>6</sup>A peaks and RNA expression, differentially expressed genes in DMSO and drug treatment groups from the m<sup>6</sup>A-Seq data were identified (Supplementary Figs. 29c–34c), which there were differences in the overall upregulation or downregulation of each group under different drug treatments, such as more upregulated genes under DOX treatment (Supplementary Fig. 32c), and less gene expression changes under LMB treatment (Supplementary Fig. 29c). Since drugs may regulate gene expression in a m<sup>6</sup>A-dependent manner, further analysis of the transcriptional abundance of each RNA under significant changes in m<sup>6</sup>A is crucial for studying methylation patterns. Here, we focused more on whether the sequencing results of the change patterns of the m<sup>6</sup>A RNA panel were consistent with PREEM imaging, so we analyzed m<sup>6</sup>A-Seq and RNA-Seq results by using the integrative genomics viewer tool to compare the changes in kurtosis (Supplementary Figs. 29d–34d). Taking Rhein treatment as an example, the peaks of m<sup>6</sup>A-containing transcripts showed a slight upregulation trend, while the majority of genes showed a more significant downregulation at transcription level (Supplementary Fig. 30d). Even though some genes were insensitive to be dysregulated upon drug treatment (whether at m<sup>6</sup>A or RNA levels), the data from the m<sup>6</sup>A-Seq and RNA-Seq were consistent with PREEM after comparison, indicating the reliability of PREEM imaging. Therefore, PREEM provides a protocol for the analysis of RNA methylation expression and spatial distribution patterns to better explain the global RNA methylation landscapes after drug treatment.

The observed fluctuations suggest a potential mechanism where drug treatment may affect the expression of transport proteins, thus modulating the nuclear export of m<sup>6</sup>A RNAs to regulate tumor cell

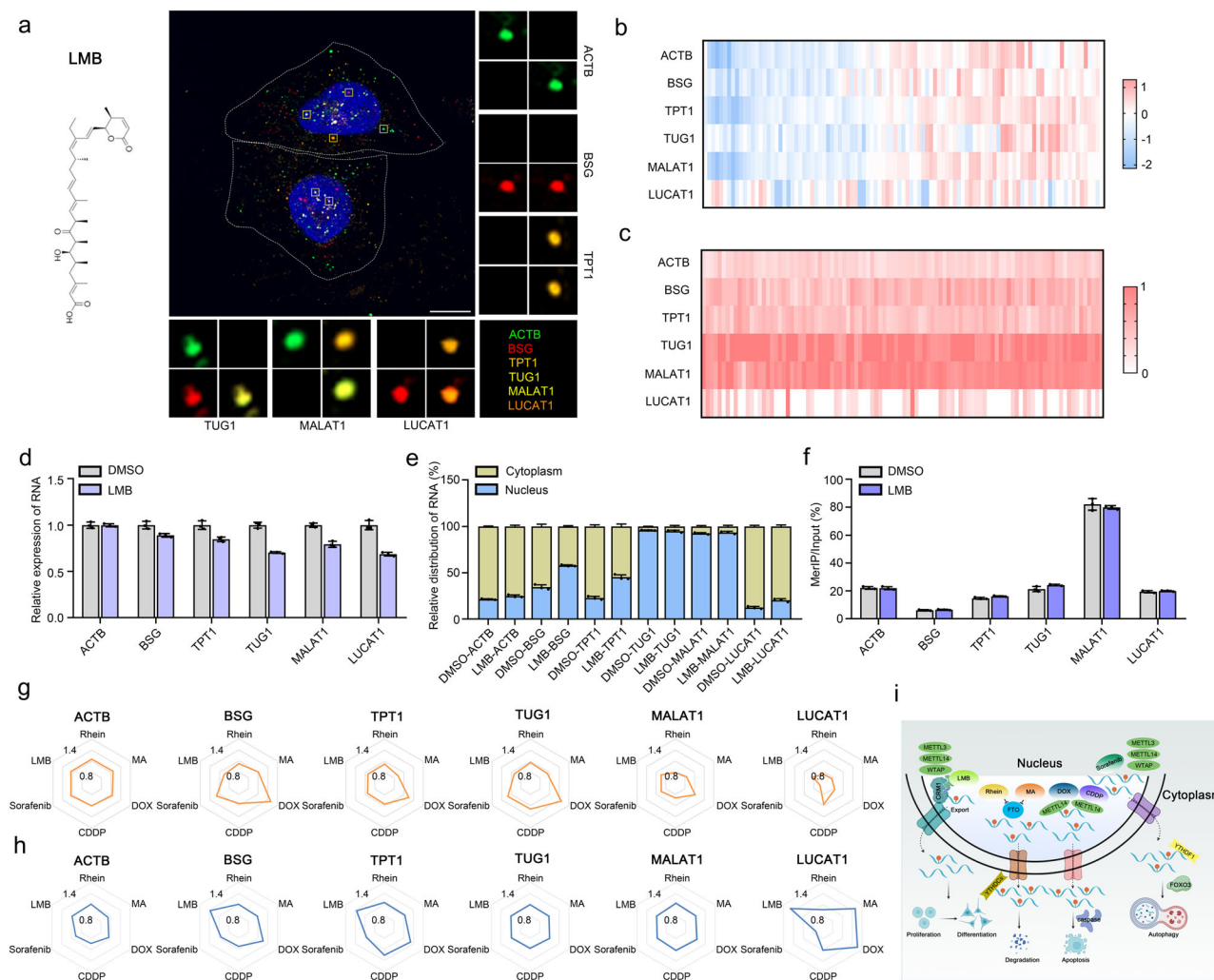


**Fig. 6 | Expression and spatial distribution changes of m<sup>6</sup>A RNAs with drug treatment revealed by PREEM in HeLa cells.** **a** Fluorescence images of six m<sup>6</sup>A RNA level visualized by PREEM in HeLa cells with LMB treated ( $N = 100$ ).  $N$  represents the number of single cells. Scale bars: 10  $\mu$ m. **b** Heat map showing the expression pattern of six m<sup>6</sup>A RNAs in HeLa cells treated with LMB by analyzing the images obtained through PREEM. **c** Heat map showing the subcellular distribution of six m<sup>6</sup>A RNAs in HeLa cells treated with LMB by analyzing the images obtained through PREEM. **d** Quantitative analysis of the expression of six RNAs in HeLa cells with LMB, measured by RT-qPCR. **e** Quantification of the relative subcellular

distribution of six RNAs in HeLa cells treated with LMB, measured by RT-qPCR. **f** MeRIP-qPCR results to quantify the relative m<sup>6</sup>A level of six RNAs in HeLa cells treated with LMB. **g** Radar charts showing expression changes of six m<sup>6</sup>A RNAs with different drug treatments compared to DMSO treated cells. **h** Radar charts showing distribution changes of six m<sup>6</sup>A RNAs with different drug treatments compared to DMSO treated cells. **i** Potential mechanism of the effects of different drug treatments on six m<sup>6</sup>A RNAs. Data are presented as mean values  $\pm$  s.d. Error bars represent the standard deviation of three independent experiments. Source data are provided as a Source Data file.

proliferation, apoptosis or differentiation (Fig. 6i). In the process of affecting tumor progression, different drugs correspond to different core proteins, but the same thing is that m<sup>6</sup>A modification plays an important role in these processes. For example, previous studies suggest that RNA transcripts with m<sup>6</sup>A modifications tend to be regulated by YTHDFs or IGF2BPs for promoting RNA stability<sup>48</sup>, while some results showed the opposite trend, implying that there might be other pathways for RNA decay under high m<sup>6</sup>A expression conditions. In order to determine the effect of m<sup>6</sup>A after drug treatment more specifically, we identified differentially activated biological processes through sequencing data. Under different drug treatments, the significant genes were related with various biological processes (Supplementary Figs. 29e–34e). For example, after treatment with LMB, significant biological changes were almost associated with intracellular transport, including RNA localization, protein localization to nucleus, nucleocytoplasmic transport, and so on (Supplementary Fig. 29e). Consistent with PREEM imaging results (Fig. 6a, e), sequencing analysis also confirmed our above speculation, demonstrating the feasibility of

PREEM. Based on the profile changes indicated by PREEM, along with insights from previous studies, potential connections between drugs and related genes is expected to be clearly revealed.

### Enhancing multiplexed imaging with reversible PREEM-based cyclic imaging

To further increase the multiplexing capacity of our method, one potential strategy is endowed PREEM with reversible capability, which has been well demonstrated in highly multiplexed FISH methods. In this work, we followed the same principle which was successfully implemented in CAD-HCR before<sup>22</sup>, that is, an extra region was placed at the 3'-terminal of the hairpins for assembly as a reversible HCR. The HCR assemblies could be disassembled when adding washers, implementing gentle erasure of fluorescence signals (Fig. 7a). The PREEM combined with reversible HCR opens the door to higher throughput imaging, as illustrated in Fig. 7b. In detail, PH1-tagged m<sup>6</sup>A antibody and all PH2 corresponding to each RNA target were incubated with the cells simultaneously to label. In the first imaging cycle, two-bit, three-

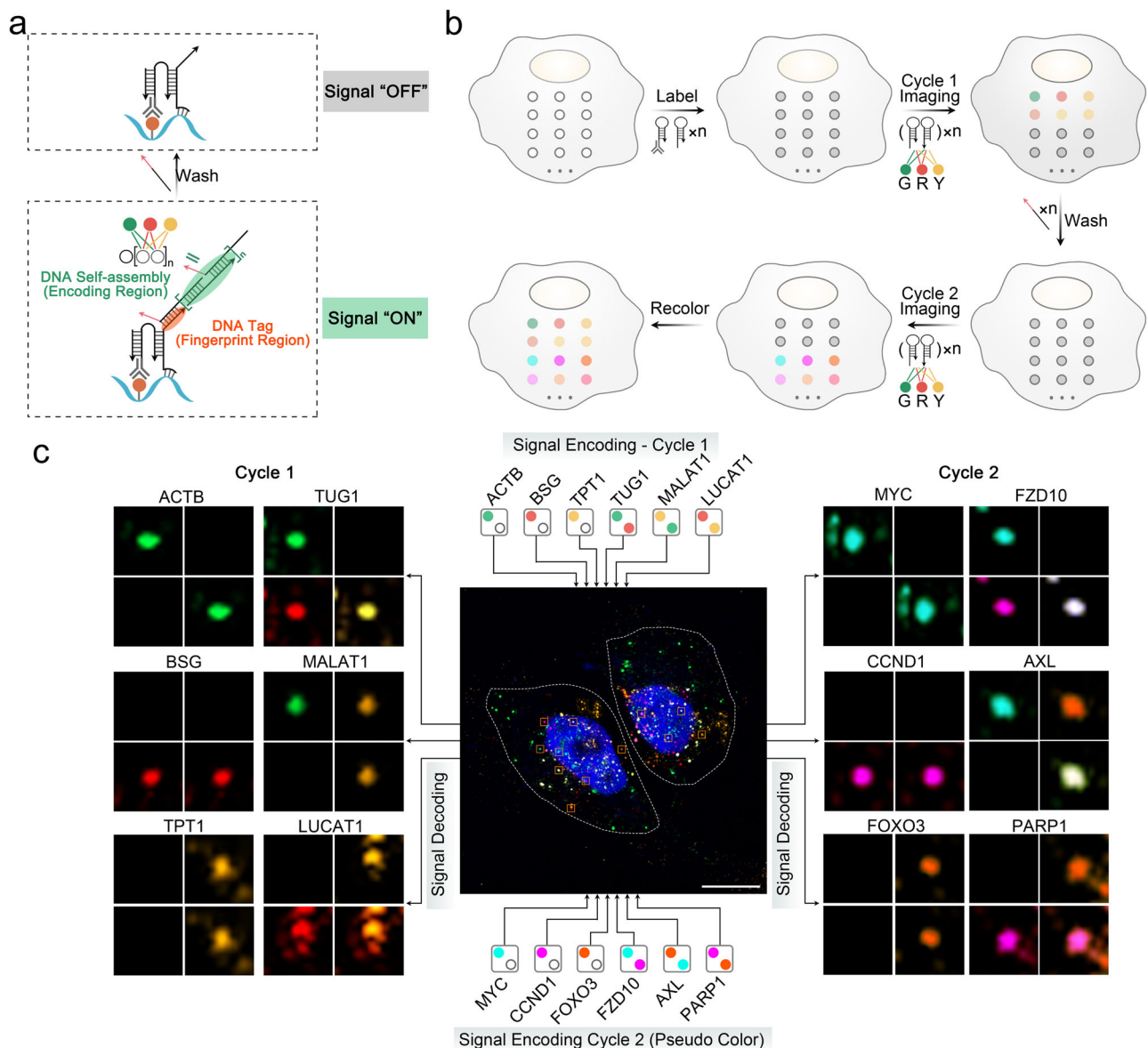


**Fig. 7 | Multiplexed imaging of m<sup>6</sup>A RNAs with reversible PREEM-based cyclic imaging.** **a** Schematic illustration of reversible PREEM. **b** Workflow of the application of reversible PREEM for multiplexed imaging of m<sup>6</sup>A RNAs. **c** Representative

fluorescence images for the spatial distribution of 12 m<sup>6</sup>A RNAs in HeLa cells (N = 100). N represents the number of single cells. Scale bars: 10  $\mu$ m.

fluorophore encoding was applied for six m<sup>6</sup>A RNAs imaging. After adding washers, the HCR assemblies were expected to disassemble into fragments. Then, the second imaging cycle could be conducted by using another set of corresponding HCRs. After "n" cycles, 6 × n m<sup>6</sup>A RNAs could be imaged, and one comprehensive image with various m<sup>6</sup>A RNAs within a single cell could be obtained by recoloring and aligning these images generated through several cycles.

We then performed a proof-of-concept experiment by using reversible PREEM with two rounds imaging processes. According to the m<sup>6</sup>A target gene database (m6A2Target) and m<sup>6</sup>A site database (SRAMP)<sup>49,50</sup>, we chose six additional m<sup>6</sup>A RNAs (MYC, CCND1, FOXO3, FZD10, AXL, and PARP1) as representative models and designed corresponding probes for imaging. As shown in Supplementary Fig. 35, we still used the same fluorophores to image and count the number of amplicons for the six new targets in turn, and after determining their feasibility, we further achieved simultaneous imaging analysis of the six m<sup>6</sup>A RNAs (Supplementary Fig. 36). Similar to the six m<sup>6</sup>A RNAs analyzed earlier, there was also a significant cell-to-cell variation in

expression and distribution for these new m<sup>6</sup>A RNAs, indicating potential for subsequent analysis. Subsequently, we investigated the ability of reversible PREEM for expanded multiplexed imaging. The fluorescence signals for six m<sup>6</sup>A RNAs (ACTB, BSG, TPT1, TUG1, MALAT1, and LUCAT1) in the first-cycle imaging were effectively removed and re-color process were also achieved without affecting the fluorescence intensity, suggesting that the signal outputs were stable across cycles (Supplementary Fig. 37). As shown in Supplementary Fig. 38, through adding the washer probes to compete with hairpins for disassembling HCR into fragments, the residual signal was reduced to less than 10% based on the statistical analysis of mean fluorescence intensity, indicating the feasibility of elution and providing a basis for subsequent cyclic imaging. Therefore, six m<sup>6</sup>A RNAs (ACTB, BSG, TPT1, TUG1, MALAT1, and LUCAT1) were imaged in the first-cycle and six other m<sup>6</sup>A RNAs (MYC, CCND1, FOXO3, FZD10, AXL, and PARP1) in the second-cycle were further conducted (Fig. 7c). These results hold the potential for the imaging of 12 (6 + 6) and even more m<sup>6</sup>A RNAs in single cells. Despite more systematic assessments are still required for



the higher multiplexed version of reversible PREEM, this innovative strategy can already meet the needs of many RNA epigenetic modification studies.

## Discussion

In this study, we have developed a strategy termed PREEM, which enables highly multiplexed, spatially resolved visualization of RNA epigenetic modifications at the single-molecule resolution level in single-cells. Our approach primarily relies on “AND” Boolean logic recognition-based proximity exchange reactions and subsequent HCR-based multichroma encoding. This exquisite design eliminates non-specific amplification, and realizes in-situ multiplexed imaging of RNA epigenetic modifications with limited fluorescence channels, improving the accessibility of PREEM in epigenetic research. As a proof-of-concept demonstration, m<sup>6</sup>A RNAs was selected as our target models. Firstly, we demonstrated the remarkable customizability of the probes within the PREEM system, enabling highly orthogonal in situ imaging of specific m<sup>6</sup>A RNAs at single-molecule resolution. Highly orthogonal recognition is achieved through the utilization of “AND” Boolean logic recognition of RNA sequence and m<sup>6</sup>A modification. Then, we evaluated the sensitivity of PREEM in response to RNA methylation regulation in cells, revealing the intercellular heterogeneity and regulatory patterns of m<sup>6</sup>A RNAs. Finally, PREEM was applied to multiple imaging of m<sup>6</sup>A RNAs using 6 targets per cycle manner. The copy numbers and distribution of six m<sup>6</sup>A RNAs in single cells were simultaneously detected, thereby shedding light on the multi-target distribution patterns and their drug response patterns to drugs within individual cells. It is beneficial for studying the synergic or antagonistic interaction among these diverse m<sup>6</sup>A RNAs.

While the demonstrated throughput is relatively limited, the multiplexing capability of PREEM can be improved with the adoption of different encoding strategies. In theory, it can be roughly divided into two categories. One simple strategy is to increase the types of fluorophores. However, the numbers of commercially available fluorophores are limited and conventional confocal microscopy will cause spectral overlap. Hyperspectral imaging can distinguish fluorescence in different wavelength ranges<sup>51</sup>, but considering the upper limit of fluorophores still restricted the numbers of practically available signal channels. Another strategy is to develop the multi-hairpin HCR mediated fluorescence encoding, breaking through the limit of 2-bit encoding. For example, through setting different proportion combinations of four fluorophores in 4-bit (four hairpin mediated HCR), we can obtain 51 cases. When fixing the number of fluorophores, the more bits (hairpin probes in HCR), the more combinations will be generated. But it is worth noting that the specificity and stability of HCR will be lower upon more hairpin assembly, leading to undesirable encoding results<sup>52</sup>.

Furthermore, PREEM offers the versatility to be readily extended to explore various RNA epigenetic transcriptional modifications beyond m<sup>6</sup>A. The key requirement is the availability of modification-specific antibodies, which are typically accessible. Building upon this foundation, PREEM can be seamlessly adapted for the simultaneous analysis of multiple RNA epigenetic transcriptome modifications. This potential extends our capacity to investigate synergistic or antagonistic effects between different RNA epigenetic transcriptome modifications, resulting in a deeper understanding of their combined impact on gene regulation. Beyond its application in single-cell research, PREEM holds promise for broader utilization in tissue-wide panoramic analyses. By venturing into tissue-level investigations, PREEM has the potential to unlock new insights into epigenetics, offering a holistic view of epigenetic landscapes across diverse cell populations within tissues.

In summary, this study describes a sequencing-free and cell-lysis-free approach for the quantitative and localization analysis of different m<sup>6</sup>A RNAs. The isothermal reaction conditions of PREEM are conducive to the preservation of cellular structure and morphology, and

the specific encoding principles allows us to identify m<sup>6</sup>A RNAs with single-molecule resolution. Although the spatial overlap of multiple amplicons might exist in intracellular environments, especially for highly multiplexed detection, the super-resolution fluorescence imaging<sup>53</sup> and expansion microscopy<sup>54</sup> would overcome the optical crowding and facilitate the discrimination of the closely located m<sup>6</sup>A RNAs. More importantly, PREEM can be applied to investigate cell-to-cell variation and spatial pattern, and has the potential to decipher post-transcription function and translational control mechanism in different cellular processes and disease occurrence in the future. We expect that PREEM will provide valuable insights required for precision biology, precision diagnosis and personalized healthcare.

## Methods

### Ethical statement

This research complies with all relevant ethical regulations. All the experiments in this research were approved by the Animal Research Ethics Committee of Shanghai Tenth People's Hospital (SHDSYY-2022-6118).

### Materials and reagents

The DNA oligonucleotides and m<sup>6</sup>A modified RNA sequences (shown in Supplementary Table 1) were synthesized by Sangon Biotechnology Inc. (Shanghai, China) and purified by high-performance liquid chromatography (HPLC). RiboLock RNase inhibitor were purchased from Life Technologies (Carlsbad, CA). NHS-PEG<sub>4</sub>-Azide (N<sub>3</sub>) and the 6×DNA gel loading dye were obtained from Thermo Fisher Scientific. Streptavidin-coated magnetic microbeads (1 μm) were purchased from New England Biolabs, Inc. (Beijing, China). Saline-sodium citrate buffer (SSC) (Ambion, AM9763), the anti-m<sup>6</sup>A antibody was purchased from Synaptic Systems, and the secondary antibody of rabbit IgG (Alexa Fluor 488) were purchased from Abcam Co., Ltd (Cambridge, MA, USA). Other chemical reagents were of analytical grade and were purchased from Sigma Aldrich (St. Louis, MO, USA). All solutions were prepared with Milli-Q water (18.2 MΩ cm<sup>-1</sup>) from a Milli-Q purification system (Millipore, Milford, MA, USA).

### Polyacrylamide gel electrophoresis

Polyacrylamide gel electrophoresis (PAGE) was performed for the characterization of oligonucleotide samples. 10 μL of each sample with 2 μL of 6× DNA gel loading dye loading buffer was loaded onto 15% non-denaturing polyacrylamide gel and electrophoresed in 1× Tris boric acid EDTA (TBE) at 120 V for 60 min. The imaging of the gel was performed using Gel Doc XR Imaging System (Bio-Rad, USA).

### Atomic force microscope characterization

Atomic force microscope (AFM) was performed for the characterization of DNA self-assembly. The 10 μL DNA assembly product was mixed with 10 μL 20 mM MgCl<sub>2</sub> solution, and the resulting mixture was absorbed onto a smooth mica sheet and incubated for 10 min. The mica sheet was then rinsed with distilled water for 30 s, and dried with nitrogen gas. The morphological analysis of DNA assembly products was performed in a tapping mode on the Agilent 5500 (Agilent Technologies).

### Preparation of antibody-DNA conjugates

To prepare the PH1-tagged m<sup>6</sup>A antibodies, antibodies was first converted to azide: a total volume of 100 μL solution containing 1 mg/mL anti-m<sup>6</sup>A antibody and 0.2 mM NHS-PEG<sub>4</sub>-N<sub>3</sub>. The reaction was performed at 4 °C for 2 h while shaking (1000 rpm). After that, azide-functionalized antibodies were purified by ultrafiltration centrifugation for 3 rounds to separate out redundant NHS-PEG<sub>4</sub>-N<sub>3</sub>. Then, azide-functionalized antibodies were reacted with DBCO-PH1 probes at a molar ratio of 1:10, and the mixed solution was incubated for 1 day at 4 °C while shaking at 1000 rpm. Finally, excess DBCO-PH1

probes were removed by ultrafiltration, and the PH1-tagged antibodies were prepared and resuspended in 1× PBS. The retention of antibodies activity was verified by immunofluorescence imaging.

### Magnetic microbead-based PREEM assay

Streptavidin-coated magnetic microbeads allow the attachment of synthesized biotinylated target (different concentrations). Streptavidin-coated magnetic micro-beads were mixed with biotinylated sequences at 37 °C for 1 h before magnetic separation and washing. Then, the prepared PH1-tagged m<sup>6</sup>A antibodies were incubated, and the proximity exchanged and HCR reaction was carried out at 37 °C for different times for optimization. Finally, the magnetic microbeads were resuspended with 300 μL of 1× PBS before analysis. The fluorescence intensity of the magnetic microbeads was detected by the CytoFLEX Flow Cytometer (Beckman Coulter, USA) and the morphology was imaged with LSM 900 Zeiss confocal microscope (Zeiss, Germany). In addition, the fluorescence was obtained using a microplate reader at 485<sub>EX</sub>/525<sub>EM</sub> nm using SpectraMax M2 Multi Mode Microplate Reader (Molecular Devices, USA).

### Cell culture

HeLa cells (human cervical cancer cell, SCSP-504), HepG2 cells (human hepatoblastoma cell, SCSP-510), A549 (human lung cancer cell, SCSP-503) were obtained from Cell Bank of the Committee on Type Culture Collection of the Chinese Academy of Sciences (Shanghai, China). HeLa and HepG2 cells were cultured in Dulbecco modified Eagle medium (DMEM) (Gibco, Invitrogen) with 10% (v/v) fetal bovine serum (FBS) (Gibco, Invitrogen) and 1% (v/v) antibiotics (penicillin-streptomycin-neomycin) (Gibco, Invitrogen). A549 cells were cultured in Roswell Park Memorial Institute (RPMI) 1640 medium (Gibco, Invitrogen) with 10% (v/v) FBS and 1% (v/v) antibiotics (penicillin-streptomycin-neomycin). Cells were all cultured at 37 °C containing 5% CO<sub>2</sub> and selected at the end of the log phase. For heat shock stimulations, cells were diluted to 3 × 10<sup>6</sup> cells mL<sup>-1</sup> and cultured at 42 °C for 1 h followed by recovery at 37 °C for 6 h.

### Oligonucleotide transfection

Synthetic siRNA oligonucleotides specific for regions in the METTL3 and ACTB mRNA were designed and synthesized by GenePharma (Shanghai, China). Cells were transfected with the oligonucleotides using Lipofectamine™ 2000 transfection reagent (Invitrogen, Carlsbad, CA, USA) according to the manufacturer's procedures.

### Immunofluorescence for m<sup>6</sup>A imaging in cells

HeLa cells were collected at the end of the log phase with different treatment (target gene knockdown or drug stimulation) and seeded in Laser confocal glass-bottomed dishes at a density of 1 × 10<sup>4</sup> cells/mL in a total volume of 1 mL, followed by an incubation step at 37 °C for 24 h for better cell attachment. The cells were fixed in 4% paraformaldehyde fix solution for 15 min at room temperature (RT) and washed three times with 1× PBS for 5 min each, permeabilized in 0.5% Triton X-100 buffer for 20 min at 37 °C, rewashed three times with 1× PBS for 5 min each and blocked with 5% BSA 1 h at RT. After being washed three times with 1× PBS for 5 min each, the cells were incubated overnight at 4 °C with the primary m<sup>6</sup>A antibody diluted in 1× PBST containing 1% BSA, followed by washing three times with 1× PBS for 5 min each. The cells were then incubated with fluorophore-conjugated secondary antibodies in 1% BSA for 1 h at RT in the dark, washed with 1× PBS and then stained with DAPI for 5 min at RT. After being washed three times with 1× PBS for 5 min each, the cells were imaged using the LSM 900 confocal laser scanning microscope (Zeiss, Germany).

### PREEM for m<sup>6</sup>A RNA imaging in cells

First, cells were seeded in confocal dishes and incubated at 37 °C for 24 h, and then fixed and followed by blocking buffer (2.5 μg/μL

sonicated salmon sperm DNA, 1 μg/μL RiboLock RNase inhibitor, 2.5 mM L-Cysteine and 1× BSA), washed three times with 1× PBS. Second, 500 nM PH2 in saline-sodium citrate buffer (SSC) buffer was incubated at 37 °C overnight, followed by washing three times with 1× PBS. Third, cells were incubated with PH1-tagged m<sup>6</sup>A antibody at 37 °C for 1 h, followed by washing three times with 1× PBS. Then 500 nM PI in SSC buffer was incubated at 37 °C for 2 h, followed by washing three times with 1× PBS. Finally, HCR reaction was performed at 37 °C for 2 h in 200 μL mixture containing 100 μL 2× SSC, 10 μL H1 (10 μM), 10 μL H2 (10 μM), and 80 μL RNase-free water, followed by washing three times with 1× PBS. DAPI was used to counterstain the cell nuclei and cells were ready for confocal imaging with LSM 900 Zeiss confocal microscope (Zeiss, Germany).

For profiling the m<sup>6</sup>A RNAs in mouse liver tissues by PREEM, we selected female BALB/c nude mice (purchased from Shanghai SLAC Laboratory Animal Company, Shanghai, China), 4–5 weeks, housed in a barrier facility on a 12 h light/dark cycle at 22–24 °C and 45–55% humidity. All experiments of animal were in accordance with the guidelines on the use and care of laboratory animals for biomedical research published by the National Institutes of Health, and approved by the the Animal Research Ethics Committee of Shanghai Tenth People's Hospital (SHDSYY-2022-6118). PREEM imaging was performed on paraffin-embedded sections from mouse liver tissues (*n* = 3). After deparaffinization and hydration, tissues sections were sequentially subjected to antigen retrieval and blocking of endogenous peroxidase. The subsequent steps remained the same as before, and we selected ACTB, BSG, and TPT1 probes for imaging. Representative images were photographed with LSM 900 Zeiss confocal microscope (Zeiss, Germany).

For exploring the impact of drug treatments on m<sup>6</sup>A RNA patterns with PREEM, we treated cells with each drug at the corresponding appropriate concentration and actuation time: rhein (100 μM for 48 h), meclufenamic acid (MA) (50 μM for 24 h), doxorubicin (DOX) (10 μM for 24 h), cisplatin (CDDP) (5 μM for 24 h), sorafenib (4 μM for 48 h), and leptomycin B (LMB) (20 nM for 24 h). After drug treatment, the subsequent steps were as described above.

For reversible PREEM-based cyclic imaging, the first cycle of in situ amplified cyclic staining was performed as described above. After adding orthogonal washers (500 nM) for 1 h at 37 °C, the HCR concatemers were disassembled into fragments. Subsequently, next cycle of “staining” could be conducted by repeating the step from “adding H1 and H2”, and then imaged using LSM 900.

### Fluorescence in situ hybridization (FISH) for RNA imaging in cells

Cells were seeded in confocal dishes and incubated at 37 °C for 24 h, and then fixed and followed by commercial FISH kit (GenePharma, Shanghai) according to the manufacturer's procedures. The samples were finally imaged by LSM 900 Zeiss confocal microscope (Zeiss, Germany) and Leica STELLARIS 5 confocal microscope for colocalization analysis, and processed by Image J software.

### RNA extraction and RT-qPCR analysis

Total RNA was isolated using TRIzol reagent (Invitrogen, USA) following the manufacturer's protocol and quantified by nanodrop 2000. For analysis of RNA expression, 200–500 ng of RNA was converted to cDNA using PrimeScript™ RT Regent Kit (TAKARA, Dalian, China). Quantitative real-time PCR using TB Green™ Premix Ex Taq™ II (TAKARA, Dalian, China) was performed on a 7500 Fast Real-time PCR system (Applied Biosystems). Quantitative PCR primers sequence are listed in Supplementary Table 1. 18S was used as a normalizing gene in all experiments. The 2<sup>-ΔΔCT</sup> method was used for relative quantitation.

### Measurement of m<sup>6</sup>A level

m<sup>6</sup>A level in total RNA were detected using a commercial m<sup>6</sup>A RNA methylation quantification kit (Abcam, UK). Briefly, total RNA was

added into each well and the capture antibody solution and detection antibody solution were added according to the manufacturer's protocol. The fluorescence of each well at 530<sub>EX</sub>/590<sub>EM</sub> nm by SpectraMax M2 Multi Mode Microplate Reader (Molecular Devices, USA) was measured for m<sup>6</sup>A level.

### Quantification of RNA methylation with m<sup>6</sup>A-IP and RT-qPCR

m<sup>6</sup>A-IP enrichment followed by RT-qPCR to quantify the m<sup>6</sup>A methylation level of the target gene was performed using Magna MeRIP m<sup>6</sup>A Kit (Millipore, MA) following the manufacturer's instructions. 5 µg of fragmented RNA extracted from HeLa cells was incubated with 5 µg m<sup>6</sup>A antibody (202003, Synaptic Systems) or mouse IgG (CS200621, Millipore)-conjugated beads in 500 µl 1× IP buffer for 4 h at 4 °C. Methylated RNA was eluted by free m<sup>6</sup>A from the beads and purified with RNeasy Mini kit (217004, Qiagen). One-tenth of the fragmented RNA was saved as an input control for standardization. The relevant enrichment of m<sup>6</sup>A of ACTB in each sample was analyzed by RT-qPCR.

### Nuclear RNA extraction and quality control

Cells were harvested at 80% density, and nuclear fractions were prepared as described in the NE-PER Nuclear and Cytoplasmic Extraction Kit (Thermo/Fisher) manufacturer's protocol, with minor modifications. 0.5 µl/ml of RNase inhibitor (Ambion/Fisher) was added to the CER1 reagent to prevent degradation. After separation from the cytoplasmic fraction, the nuclear pellet was washed twice with 1× PBS and resuspended in an appropriate volume of TRIzol reagent (Invitrogen). The nuclear pellet was homogenized with a Polytron PT 1200E. RNA was purified using the TRIzol reagent manufacturer's protocol and quantified using the Quant-iT RNA HS Assay Kit (Invitrogen). The efficiency of separation was determined by measuring nuclear and cytoplasmic RNA fractions by qRT-PCR for the relative quantities of nuclear (U6) or cytoplasmic (GAPDH) control genes.

### High throughput m<sup>6</sup>A sequencing

Total RNA was extracted from HeLa cells with DMSO or different drug treatment. RNA was tested for quality using nanodrop and gel electrophoresis. RNA was randomly fragmented to ~200 nucleotides by RNA fragmentation reagents. Fragmented RNA was incubated for 2 h at 4 °C with m<sup>6</sup>A antibody (Synaptic System, Cat. No. 202003, diluted to 0.5 µg/ul) for immunoprecipitation following the standard protocol of the Magna methylated RNA immunoprecipitation (MeRIP) m<sup>6</sup>A kit (Merk Millipore, MA). The mixture was then incubated with beads and eluted with elution buffer (1× IP buffer and 6.7 mM m<sup>6</sup>A). Eluted RNA was precipitated by 75% ethanol. The eluted RNA was treated with RNasin (Ambion, Cat No. AM2694) according to the manufacturer's instructions. TruSeq Stranded mRNA Sample Pre Kit (Illumina) was used to construct the library from immunoprecipitated RNA and input RNA following a published protocol. Sequencing was performed on an Illumina HiSeq machine with 2× 100 cycles Solexa paired-end sequencing. The sequencing service and subsequent bioinformatics analysis were supported by Cloud-Seq Biotech Ltd Co. (Shanghai, China).

### Statistical analysis

All the data were presented as mean ± standard deviation. Differences between two groups or multiple groups were analyzed by Student's *t*-test and one-way analysis of variance (ANOVA), respectively. Statistical analyses were performed using the GraphPad Prism 8.0 (GraphPad Software, La Jolla, CA, USA). Difference with *p* < 0.05 was considered to statistically significant. For fluorescence images by LSM 900 Zeiss confocal microscope, bright spots were distinguished from the background by setting the threshold value, and the copy number of amplicons were determined by particle analysis in Image J software.

### Reporting summary

Further information on research design is available in the Nature Portfolio Reporting Summary linked to this article.

### Data availability

The data supporting the findings of this study are available from the corresponding authors upon request. The seq data were deposited in GEO dataset with the accession number GSE280639. Source data for the figures are provided with this paper. Source data are provided with this paper.

### Code availability

The specific codes of computer aided design program have been deposited on Zenodo (<https://doi.org/10.5281/zenodo.5520160>).

### References

- Gu, C. et al. RNA m(6)A modification in cancers: molecular mechanisms and potential clinical applications. *Innovation* **1**, 100066 (2020).
- Yang, Y., Hsu, P. J., Chen, Y. S. & Yang, Y. G. Dynamic transcriptomic m(6)A decoration: writers, erasers, readers and functions in RNA metabolism. *Cell Res.* **28**, 616–624 (2018).
- Dominissini, D. et al. Topology of the human and mouse m6A RNA methylomes revealed by m6A-seq. *Nature* **485**, 201–206 (2012).
- Huang, H., Weng, H. & Chen, J. m(6)A modification in coding and non-coding RNAs: roles and therapeutic implications in cancer. *Cancer Cell* **37**, 270–288 (2020).
- Shafik, A. M. et al. N6-methyladenosine dynamics in neurodevelopment and aging, and its potential role in Alzheimer's disease. *Genome Biol.* **22**, 17 (2021).
- Weibrecht, I. et al. In situ detection of individual mRNA molecules and protein complexes or post-translational modifications using padlock probes combined with the in situ proximity ligation assay. *Nat. Protocols* **8**, 355–372 (2013).
- Konno, M. et al. Distinct methylation levels of mature microRNAs in gastrointestinal cancers. *Nat. Commun.* **10**, 3888 (2019).
- Ge, L. et al. Level of N6-methyladenosine in peripheral blood RNA: a novel predictive biomarker for gastric cancer. *Clin. Chem.* **66**, 342–351 (2020).
- Helm, M. & Motorin, Y. Detecting RNA modifications in the epitranscriptome: predict and validate. *Nat. Rev. Genet.* **18**, 275–291 (2017).
- Cui, X., Meng, J., Zhang, S., Chen, Y. & Huang, Y. A novel algorithm for calling mRNA m6A peaks by modeling biological variances in MeRIP-seq data. *Bioinformatics* **32**, i378–i385 (2016).
- Li, Y. et al. Single-cell m(6)A mapping in vivo using picoMeRIP-seq. *Nat. Biotechnol.* **42**, 591–596 (2023).
- Xiao, Y. et al. An elongation- and ligation-based qPCR amplification method for the radiolabeling-free detection of locus-specific N6-methyladenosine modification. *Angew. Chem. Int. Ed.* **57**, 15995–16000 (2018).
- McIntyre, A. B. R. et al. Limits in the detection of m6A changes using MeRIP/m6A-seq. *Sci. Rep.* **10**, 6590 (2020).
- Ren, X. et al. Single-cell imaging of m(6) A modified RNA using m(6) A-specific in situ hybridization mediated proximity ligation assay (m(6) AISH-PLA). *Angew. Chem. Int. Ed. Engl.* **60**, 22646–22651 (2021).
- Sheehan, C. J., Marayati, B. F., Bhatia, J. & Meyer, K. D. In situ visualization of m6A sites in cellular mRNAs. *Nucleic Acids Res.* **51**, e101 (2023).
- Choi, H. M. et al. Programmable in situ amplification for multiplexed imaging of mRNA expression. *Nat. Biotechnol.* **28**, 1208–1212 (2010).
- Ma, H. et al. Multiplexed labeling of genomic loci with dCas9 and engineered sgRNAs using CRISPRainbow. *Nat. Biotechnol.* **34**, 528–530 (2016).



18. Ma, H. et al. CRISPR-Sirius: RNA scaffolds for signal amplification in genome imaging. *Nat. Methods* **15**, 928–931 (2018).
19. Liu, X. et al. Aptamer based probes for living cell intracellular molecules detection. *Biosens. Bioelectron.* **208**, 114231 (2022).
20. Marras, S. A. E., Bushkin, Y. & Tyagi, S. High-fidelity amplified FISH for the detection and allelic discrimination of single mRNA molecules. *Proc. Natl Acad. Sci. USA* **116**, 13921–13926 (2019).
21. Chen, K. H., Boettiger, A. N., Moffitt, J. R., Wang, S. & Zhuang, X. Spatially resolved, highly multiplexed RNA profiling in single cells. *Science* **348**, aaa6090 (2015).
22. Liu, X. et al. Computer-aided design of reversible hybridization chain reaction (CAD-HCR) enables multiplexed single-cell spatial proteomics imaging. *Sci. Adv.* **8**, eabk0133 (2022).
23. Fu, Y., Dominissini, D., Rechavi, G. & He, C. Gene expression regulation mediated through reversible m<sup>6</sup>A RNA methylation. *Nat. Rev. Genet.* **15**, 293–306 (2014).
24. Roundtree, I. A., Evans, M. E., Pan, T. & He, C. Dynamic RNA modifications in gene expression regulation. *Cell* **169**, 1187–1200 (2017).
25. Ghani, M., Sato, C. & Rogaeva, E. Segmental duplications in genome-wide significant loci and housekeeping genes; warning for GAPDH and ACTB. *Neurobiol. Aging* **34**, 1710.e1711–1710.e1714 (2013).
26. Jin, J., Zhu, C., Wang, J., Zhao, X. & Yang, R. The association between ACTB methylation in peripheral blood and coronary heart disease in a case-control study. *Front. Cardiovasc. Med.* **9**, 972566 (2022).
27. Liu, N. et al. Probing N<sup>6</sup>-methyladenosine RNA modification status at single nucleotide resolution in mRNA and long noncoding RNA. *RNA* **19**, 1848–1856 (2013).
28. Sivasudhan, E., Blake, N., Lu, Z. L., Meng, J. & Rong, R. Dynamics of m<sup>6</sup>A RNA methylome on the hallmarks of hepatocellular carcinoma. *Front. Cell Dev. Biol.* **9**, 642443 (2021).
29. Zhang, H. et al. Dynamic landscape and evolution of m<sup>6</sup>A methylation in human. *Nucleic Acids Res.* **48**, 6251–6264 (2020).
30. Richter, K., Haslbeck, M. & Buchner, J. The heat shock response: life on the verge of death. *Mol. Cell* **40**, 253–266 (2010).
31. Zhou, J. et al. Dynamic m<sup>6</sup>A mRNA methylation directs translational control of heat shock response. *Nature* **526**, 591–594 (2015).
32. Fan, L. et al. METTL3-mediated N<sup>6</sup>-methyladenosine methylation modifies Foxp3 mRNA levels and affects the Treg cells proportion in peripheral blood of patients with asthma. *Ann. Clin. Lab Sci.* **52**, 884–894 (2022).
33. Wu, Y. et al. Mettl3-mediated m(6)A RNA methylation regulates the fate of bone marrow mesenchymal stem cells and osteoporosis. *Nat. Commun.* **9**, 4772 (2018).
34. Wang, P., Dostader, K. A. & Nam, Y. Structural basis for cooperative function of Mettl3 and Mettl14 methyltransferases. *Mol. Cell* **63**, 306–317 (2016).
35. Yang, H. et al. Hypoxia inducible lncRNA-CBSLR modulates ferroptosis through m<sup>6</sup>A-YTHDF2-dependent modulation of CBS in gastric cancer. *J. Adv. Res.* **37**, 91–106 (2022).
36. Li, Q. et al. HIF-1 $\alpha$ -induced expression of m<sup>6</sup>A reader YTHDF1 drives hypoxia-induced autophagy and malignancy of hepatocellular carcinoma by promoting ATG2A and ATG14 translation. *Signal Transduct. Target Ther.* **6**, 76 (2021).
37. Das, S., Vera, M., Gandin, V., Singer, R. H. & Tutucci, E. Intracellular mRNA transport and localized translation. *Nat. Rev. Mol. Cell Biol.* **22**, 483–504 (2021).
38. Chen, L. L. Linking long noncoding RNA localization and function. *Trends Biochem. Sci.* **41**, 761–772 (2016).
39. Wang, T., Kong, S., Tao, M. & Ju, S. The potential role of RNA N<sup>6</sup>-methyladenosine in Cancer progression. *Mol. Cancer* **19**, 88 (2020).
40. Lan, Q. et al. The emerging roles of RNA m(6)A methylation and demethylation as critical regulators of tumorigenesis, drug sensitivity, and resistance. *Cancer Res.* **81**, 3431–3440 (2021).
41. Liu, S. et al. M6AREG: m<sup>6</sup>A-centered regulation of disease development and drug response. *Nucleic Acids Res.* **51**, D1333–D1344 (2023).
42. Yu, J. et al. Dynamic m<sup>6</sup>A modification regulates local translation of mRNA in axons. *Nucleic Acids Res.* **46**, 1412–1423 (2018).
43. Huang, Y. et al. Meclofenamic acid selectively inhibits FTO demethylation of m<sup>6</sup>A over ALKBH5. *Nucleic Acids Res.* **43**, 373–384 (2015).
44. Weaver, D. A. et al. ABCC5, ERCC2, XPA and XRCC1 transcript abundance levels correlate with cisplatin chemoresistance in non-small cell lung cancer cell lines. *Mol. Cancer* **4**, 18 (2005).
45. Esawie, M., Louka, M. L., Hasanin, A. H., El-Kholi, A. A. & Said Ali, H. High-glucose-induced hyperosmolar stress sensitizes HepG2 cell lines to sorafenib. *Gene* **844**, 146828 (2022).
46. Tsuchiya, A., Tashiro, E., Yoshida, M. & Imoto, M. Involvement of nuclear accumulation of heat shock protein 27 in leptomycin B-induced apoptosis in HeLa cells. *J. Antibiot.* **58**, 810–816 (2005).
47. Edens, B. M. et al. FMRP modulates neural differentiation through m(6)A-dependent mRNA nuclear export. *Cell Rep.* **28**, 845–854 e845 (2019).
48. Shen, C. et al. M<sup>6</sup>A-dependent glycolysis enhances colorectal cancer progression. *Mol. Cancer* **19**, 72 (2020).
49. Deng, S. et al. M6A2Target: a comprehensive database for targets of m<sup>6</sup>A writers, erasers and readers. *Brief Bioinform.* **22**, bbaa055 (2021).
50. Zhou, Y., Zeng, P., Li, Y. H., Zhang, Z. & Cui, Q. SRAMP: prediction of mammalian N<sup>6</sup>-methyladenosine (m<sup>6</sup>A) sites based on sequence-derived features. *Nucleic Acids Res.* **44**, e91 (2016).
51. Leavesley, S. J. et al. Hyperspectral imaging fluorescence excitation scanning for colon cancer detection. *J. Biomed. Opt.* **21**, 104003 (2016).
52. Yu, C., Wang, Y., Wu, R., Zhu, Z. & Li, B. Study on the functionalization and signaling efficiency of the hybridization chain reaction using traditional and single molecular characterizations. *ACS Appl. Bio Mater.* **4**, 3649–3657 (2021).
53. Lubeck, E. & Cai, L. Single-cell systems biology by super-resolution imaging and combinatorial labeling. *Nat. Methods* **9**, 743–748 (2012).
54. Chen, F. et al. Nanoscale imaging of RNA with expansion microscopy. *Nat. Methods* **13**, 679–684 (2016).

## Acknowledgements

This work was supported by the National Key Research and Development Program of China (2023YFC2606100 to Xiaoli Zhu), the National Natural Science Foundation of China (Grant Nos. 32371531 and 22074090 to Xiaoli Zhu, 82293662 and 82172357 to Qihui Pan, 32301256 to Dongsheng Mao, 82102477 to Song Hu), the Medical Innovation Research Special Project of the Shanghai Science and Technology Innovation Action Plan (23Y11907900 to Xiaoli Zhu), the Key Project of Shanghai “Science and Technology Innovation Action Plan” (22JC1402300 and 21JC1406602 to Qihui Pan), the Shanghai Sailing Program (23YF1432600 to Dongsheng Mao), and the Natural Science Foundation of Shanghai (23ZR1449100 to Dongsheng Mao), the Shanghai Municipal Health Commission (20234Y0005 to Dongsheng Mao).

## Author contributions

Conceptualization, X.Z., Q.P., and B.S.; methodology, X.Z., X.T., D.M., and W.L.; investigation, X.T., D.M., R.Z., and S.H.; visualization, D.M., H.G., P.Z., and W.L.; acquisition, Q.P. and B.S.; supervision, X.Z., Q.P., and B.S.; writing-original draft, X.T., and D.M.; writing-review & editing, X.Z., X.T., and D.M. All authors contributed to the final text of the paper.

## Competing interests

The authors declare no competing interests.

## Additional information

**Supplementary information** The online version contains supplementary material available at <https://doi.org/10.1038/s41467-025-56331-w>.

**Correspondence** and requests for materials should be addressed to Wenxing Li, Qiuhui Pan, Bing Shen or Xiaoli Zhu.

**Peer review information** *Nature Communications* thanks the anonymous reviewers for their contribution to the peer review of this work. A peer review file is available.

**Reprints and permissions information** is available at <http://www.nature.com/reprints>

**Publisher's note** Springer Nature remains neutral with regard to jurisdictional claims in published maps and institutional affiliations.

**Open Access** This article is licensed under a Creative Commons Attribution-NonCommercial-NoDerivatives 4.0 International License, which permits any non-commercial use, sharing, distribution and reproduction in any medium or format, as long as you give appropriate credit to the original author(s) and the source, provide a link to the Creative Commons licence, and indicate if you modified the licensed material. You do not have permission under this licence to share adapted material derived from this article or parts of it. The images or other third party material in this article are included in the article's Creative Commons licence, unless indicated otherwise in a credit line to the material. If material is not included in the article's Creative Commons licence and your intended use is not permitted by statutory regulation or exceeds the permitted use, you will need to obtain permission directly from the copyright holder. To view a copy of this licence, visit <http://creativecommons.org/licenses/by-nc-nd/4.0/>.

© The Author(s) 2025